

1 **Did high Neo-Tethys subduction rates contribute to early Cenozoic warming?**

2

3 **FINAL VERSION OF ACCEPTED MANUSCRIPT – 4/11/2015**

4

5 Guilhem Hoareau^{1,2}, Brahimsamba Bomou^{1,3,4}, Douwe J.J. van Hinsbergen⁵, Nicolas Carry¹,
6 Didier Marquer¹, Yannick Donnadiou⁴, Guillaume Le Hir³, Bruno Vrielynck⁶ and Anne-
7 Véronique Walter-Simonnet¹

8

9 ¹UMR 6249 Chrono-environnement (CNRS-Université de Franche-Comté), F-25030 Besançon
10 cedex, France

11 ²UMR CNRS TOTAL 5150 Laboratoire des Fluides Complexes et leurs Réservoirs, Université
12 de Pau et des Pays de l'Adour, I.P.R.A., Avenue de l'Université BP 1155
13 F-64013 PAU cedex, France

14 ³Institut de Physique du Globe de Paris, 4 place Jussieu 75005 Paris, France

15 ⁴LSCE/UVSQ/IPSL CEA Saclay, Orme des Merisiers, F-91191 Gif-sur-Yvette, France

16 ⁵Department of Earth Sciences, Utrecht University, Budapestlaan 4, 3584 CD Utrecht, the
17 Netherlands

18 ⁶UMR 7193 – ISTEP (CNRS-UPMC), 4 place Jussieu, F-75252 Paris cedex 05, France

19

20

21 **ABSTRACT**

22 The 58-51 Ma interval was characterized by a long-term increase of global temperatures (+4 to
23 +6°C) up to the Early Eocene Climate Optimum (EECO, 52.9-50.7 Ma), the warmest interval of

24 the Cenozoic. It was recently suggested that sustained high atmospheric $p\text{CO}_2$, controlling warm
25 early Cenozoic climate, may have been released during Neo-Tethys closure through the
26 subduction of large amounts of pelagic carbonates and their recycling as CO_2 at arc volcanoes.
27 To analyze the impact of Neo-Tethys closure on early Cenozoic warming, we have modeled the
28 volume of subducted sediments and the amount of CO_2 emitted along the northern Tethys
29 margin. The impact of calculated CO_2 fluxes on global temperature during the early Cenozoic
30 have then been tested using a climate carbon cycle model (GEOCLIM). We show that CO_2
31 production may have reached up to 1.55×10^{18} mol/Ma specifically during the EECO, ~4 to 37%
32 higher than the modern global volcanic CO_2 output, owing to a dramatic India-Asia plate
33 convergence increase. The subduction of thick Greater Indian continental margin carbonate
34 sediments at ~55-50 Ma may also have led to additional CO_2 production of 3.35×10^{18} mol/Ma
35 during the EECO, making a total of 85% of the global volcanic CO_2 outgassed. However,
36 climate modeling demonstrates that timing of maximum CO_2 release only partially fit with the
37 EECO, and that corresponding maximum $p\text{CO}_2$ values (750 ppm) and surface warming ($+2^\circ\text{C}$)
38 do not reach values inferred from geochemical proxies, a result consistent with conclusions arise
39 from modeling based on other published CO_2 fluxes. These results demonstrate that CO_2 derived
40 from decarbonation of Neo-Tethyan lithosphere may have possibly contributed to, but certainly
41 cannot account alone for early Cenozoic warming. Other commonly cited sources of excess CO_2
42 such as enhanced igneous province volcanism also appear to be up to one order of magnitude
43 below fluxes required by the model to fit with proxy data of $p\text{CO}_2$ and temperature at that time.
44 An alternate explanation may be that CO_2 consumption, a key parameter of the long-term
45 atmospheric $p\text{CO}_2$ balance, may have been lower than suggested by modeling. These results call
46 for a better calibration of early Cenozoic weathering rates.

47

48 1. INTRODUCTION

49 Based on paleotemperature proxies, a trend of decreasing global temperatures throughout
50 the Late Mesozoic and Cenozoic has long been identified (e.g, **Shackelton and Kennett, 1975;**
51 **Zachos et al., 2001, 2008; Cramer et al., 2009; Friedrich et al., 2012**). Climatic modeling
52 suggests that this cooling mainly results from decreasing seafloor spreading and subduction
53 rates, as well as increasing CO₂ removal through silicate weathering (**Park and Royer, 2011;**
54 **Godderis et al., 2014; van der Meer et al., 2014**). During the Cenozoic, CO₂ consumption was
55 mainly governed by the erosion of the Tethyan orogenic belt, and by continental drift,
56 responsible for the arrival of highly weatherable basaltic provinces in the equatorial belt (**Raymo**
57 **and Ruddiman, 1992; Kent and Muttoni, 2013; Lefebvre et al., 2013**). However, global
58 cooling was interrupted by a long-term increase of global temperatures (+4 to +6°C) and *p*CO₂
59 (~450 ppm to ~1000 ppm) from 58 to 50.7 Ma, crowned by the Early Eocene Climate Optimum
60 (EECO, 52.9-50.7 Ma), the warmest interval of the Cenozoic (**Zachos et al., 2001; Beerling and**
61 **Royer, 2011**). Because conventional carbon cycle models compute important weathering rates at
62 that time, they fail to reproduce this rise in temperature and atmospheric CO₂ without the
63 addition of excess CO₂ compared to background CO₂ volcanic degassing rates (4-10x10¹⁸
64 molCO₂/Ma at present; **Berner, 2004**) (**Lefebvre et al., 2013; Van der Meer et al., 2014**).
65 Carbonates also indicate that from ~58.0 to 52.5 Ma this warming was characterized by a 2 per
66 mil negative shift in marine and terrestrial δ¹³C, referred to as the Late Paleocene-Early Eocene
67 (LPEE) by **Komar et al. (2013)**. This drop in δ¹³C suggests an additional source of depleted CO₂
68 (i.e enriched in ¹²C) or/and decreased net organic carbon burial (**Hilting et al, 2008; Komar et**
69 **al. 2013**). In contrast, despite warm temperature, the EECO was associated with a rise in δ¹³C
70 (**Cramer et al., 2009**), indicative of the addition of heavy CO₂ or/and alternatively by increased

71 net organic carbon burial (e.g., **Komar et al., 2013**). Various origins of excess CO₂ have been
72 proposed for both periods of the early Cenozoic. Most invoke the activity of large igneous
73 provinces such as the North Atlantic Igneous Province (NAIP), since a mantellic source of CO₂
74 ($\delta^{13}\text{CO}_2$ ranging from -3 to -10‰) may be compatible with carbon isotope proxies for most of
75 the period of warming (see **Reagan et al. 2013** and references therein). Alternatively, **Beck et al.**
76 **(1995)**, **Hilting et al. (2008)** and **Komar et al. (2013)** proposed that large amounts of low- $\delta^{13}\text{C}$
77 organic carbon were being stored in carbon capacitors separate from the
78 ocean/atmosphere/biosphere (e.g., peat, gas hydrates, permafrost) during the Paleocene. They
79 were then massively released during the LPEE warming and progressively vanished during the
80 EECO (**Komar et al., 2013**). Finally, among several other hypotheses, it was suggested that
81 Neo-Tethys closure may have strongly controlled Cretaceous and early Cenozoic climates, up to
82 the EECO, through the subduction of tropical pelagic carbonates ($\delta^{13}\text{C} \sim 0\text{‰}$) under the Asian
83 plate and their recycling as CO₂ at arc volcanoes (**Edmond and Huh, 2003; Kent and Muttoni,**
84 **2008; Johnston et al., 2011**). These authors argued that the tropical latitudes of the northern
85 Neo-Tethys could have favoured deposition of carbonate-rich pelagic sediments on the Tethyan
86 seafloor. In detail, **Kent and Muttoni (2008)** suggested that the Indian plate dominated this
87 “carbonate subduction factory”, with a major decrease in CO₂ production as India and Asia
88 collided some 50 Ma ago. However, the same authors recently concluded for low CO₂ outgassing
89 at the Tethyan arc, mainly as a result of low decarbonation during subduction (**Kent and**
90 **Muttoni, 2013**). For **Kent and Muttoni (2013)**, high CO₂ could be explained by less efficient
91 weathering close to the EECO, rather than by additional CO₂ production.

92 In this contribution, we aim to test whether Neo-Tethyan closure, which was obviously
93 associated to widespread arc volcanism, may have had or not an impact on global warming

94 during the LPEE and the EECO, keeping in mind that this hypothesis hardly conforms to
95 available carbon isotope records during the LPEE. To this end, we first use a simple model that
96 calculates the volume of sediments subducted along with Neo-Tethyan oceanic and Greater
97 Indian margin lithospheres, and computes a range of CO₂ fluxes emitted at active arc volcanoes
98 along the northern Neo-Tethys margin. A coupled climate-carbon cycle model (GEOCLIM) is
99 then used to quantify the impact of CO₂ fluxes obtained from our model and that of **Kent and**
100 **Muttoni (2013)**, on Paleocene / Eocene *p*CO₂ and atmospheric temperature. Finally, in light of
101 our results, we discuss the relevance of alternate hypotheses commonly cited to explain the
102 LPEE and the EECO.

103

104 **2. NEO-TETHYAN HISTORY AND RELATED ARC VOLCANISM**

105 The Neo-Tethys ocean opened westward during the Permian to Triassic, separating
106 several micro-continents (e.g., Pontides, Central Iran, Central Afghanistan, Tibet, and Western
107 Burma) from Gondwana in the south (**Kazmin, 1991; Dercourt et al., 1993; Ricou, 1994;**
108 **Stampfli and Borel 2002; Muttoni et al., 2009**). These reached the southern Eurasian margin in
109 Late Triassic and younger times, followed by inception of subduction of Neo-Tethyan oceanic
110 lithosphere. In the western Neo-Tethys, convergence of Africa to Eurasia began in the Aptian
111 (**Kazmin, 1991; Dercourt et al., 1993; Ricou, 1994; Rosenbaum and Lister, 2002; Stampfli**
112 **and Borel, 2002; van Hinsbergen et al 2005**) (**Figure 1**). Neo-Tethys subduction below the
113 Iran margin started at least in Jurassic time and continued until Arabia-Eurasia collision in latest
114 Eocene-Early Oligocene time (**Agard et al., 2011; Mouthereau, 2011; McQuarrie and van**
115 **Hinsbergen, 2013**). Subduction below Tibet in the Early Cretaceous occurred simultaneously
116 with Indian separation from eastern Antarctica and Australia ~130 Ma ago (**Guillot et al., 2008;**

117 **van Hinsbergen et al., 2011a**). Collision between the northernmost continental crust of the
118 Indian plate and Eurasia is commonly stated to have started between ~60 and ~50 Ma (e.g.,
119 **Dupont-Nivet et al., 2010; Najman et al., 2010; Orme et al., 2014; Hu et al., in press**)
120 (**Figure 1**). At about the same time (~56-47 Ma), subducted Indian northern margin rocks were
121 affected by High-Pressure and Ultra-High Pressure metamorphism (up to ~100 km depth)
122 (**Guillot et al., 2008**). In the easternmost Neo-Tethys (Indonesia), **Whittaker et al. (2007)**
123 suggested that active subduction below Eurasia was active throughout the Upper Cretaceous and
124 the Cenozoic, although **Hall (2012)** proposed that Sundaland was mostly surrounded by inactive,
125 or transform margins from 90 to 45 Ma. Finally, there is also documentation for multiple intra-
126 oceanic subduction events leading to widespread ophiolite obduction, ending around 70 Ma
127 along NE Arabia, and around 55-50 Ma in SE Oman, Pakistan (**Gnos et al., 1997; Marquer et**
128 **al., 1998; Gaina et al., 2015**), and the Tibetan Himalaya (**Hébert et al., 2012; Garzanti and**
129 **Hu, 2014; Huang et al. 2015a**) (**Figure 1**).

130 Evidence of latest Cretaceous and early Cenozoic subduction-related magmatic activity is
131 widespread along, and restricted to the Eurasian margin. For example, in the Zagros mountains
132 and Turkey (Pontides), widespread arc magmatism occurred during the Mesozoic and the
133 Cenozoic (**Sengör et al., 1988; Okay and Sahinturk, 1997; Barrier and Vrielynck, 2008;**
134 **Agard et al., 2011; Eyuboglu et al., 2011**). In southern Tibet, a long-lasting volcanic
135 ‘Gangdese’ arc was active from Early Cretaceous to Eocene time (**Ji et al., 2009**), with a short-
136 lived ignimbrite flare-up stage around 50 Ma coinciding with Tibetan Himalaya-Lhasa
137 continental collision (**Ji et al., 2009**), followed by return of the arc to a background state until the
138 Late Eocene (**Sanchez et al., 2013**). In Sundaland, Paleocene-Eocene magmatism was likely
139 active since at least ~63 Ma (e.g., **McCourt et al., 1996; Bellon et al., 2004**).

140

141 **3. VOLCANIC CO₂ RELEASE DURING THE LPEE AND THE EECO BY THE**
142 **CARBONATE SUBDUCTION FACTORY MODEL (CSFM)**

143

144 CSFM is designed to calculate the amount of CO₂ produced during Neo-Tethys closure.
145 It quantifies the Neo-Tethys volcanic arc gas output as a function of subduction flux of oceanic
146 crust, pelagic sediments, and also of Indian margin sediments at the onset of Indian continental
147 lithosphere subduction. Required input parameters are subduction rate, trench length, the
148 thickness, density, carbonate and organic carbon content of sediments and oceanic crust, the
149 decarbonation efficiency of subducted material, and the time-lag to gas emission at the surface.

150

151 **3.1 Subduction rates and trench length estimates**

152 Subduction rates of African, Arabian and Indian plates below Eurasia were calculated
153 from plate motion reconstructions made with GPlates (<http://www.gplates.org/>) (Boyden et al,
154 2011) using time steps of 0.5 Ma, between 65 and 35 Ma. Given the controversy regarding the
155 presence or not of continuous subduction in easternmost Neo-Tethys from the Late Cenozoic to
156 the Eocene (Sundaland) (e.g., **Whittaker et al., 2007**; **Hall, 2012**), we did not consider
157 Australia-Eurasia convergence and assess the potential role of Neo-Tethys subduction based on
158 the central and western Neo-Tethys alone. We used the reconstructed position of three points
159 located on the western, central and eastern syntaxis of each plate, similar to **Rosenbaum and**
160 **Lister (2002)**, **Alvarez (2010)** and **van Hinsbergen et al. (2011a)**. Their present locations in
161 Lat/Long decimal coordinates are 37/15, 32/24, 24/32 (Africa), 24.1/32.9, 15.3/38.9, 23.6/58.6
162 (Arabia) and 30.5/72, 30.5/82, 23.5/92 (India). Euler rotation parameters were taken from plate

163 circuit A of **van Hinsbergen et al. (2011a)**. Because Cretaceous-Cenozoic intra-Eurasian
164 shortening north of the African-Arabian plate is limited to perhaps 200 km and focused in the
165 late Cenozoic (e.g., **Mouthereau, 2011; McQuarrie and van Hinsbergen, 2013**), we
166 considered Africa/Arabia-Eurasia convergence rates as subduction rates. For India, the
167 subduction rate was calculated subtracting intra-Asian shortening rates expressed as Euler
168 rotation parameters by **van Hinsbergen et al. (2011b)** from India-Asia convergence rates. Given
169 the uncertainties concerning the rate of subduction below widespread ophiolites, and the
170 locations of these subduction zones, we chose to simplify our scenario by assigning all
171 subduction to the zones indicated in **Figure 1**. In addition, we assume that there was no active
172 spreading within the Neo-Tethys since 65 Ma. For each plate, subduction rates at each time step
173 were corrected for convergence obliquity related to the orientation of the subduction trench
174 (**Annex 1**). Trench lengths were set to 2500 km for Africa, 2900 km for Arabia (from the Levant
175 fault to the Makran) and 2600 km for India (from the Makran to the Indo-Burma range), making
176 a total length of 8000 km (similar to **Johnston et al., 2011**) (**Figure 1**). Three ages, 55, 52.5 and
177 50 Ma, were tested for the onset of Greater Indian thinned continental lithosphere subduction
178 beneath Eurasia, corresponding to a shift from pelagic to margin sediments on the Indian plate.
179 Scenarios without India-Asia continental subduction were also run, to assess the maximum
180 potential effects of younger collision.

181

182 **3.2. Geometric and lithological parameters**

183 3.2.1. Oceanic crust and pelagic sediments

184 In the model, all oceanic lithosphere has the same crust and sediment thickness. For the
185 oceanic crust a constant thickness of 7 km and a density of 3 t/m³ were retained. Because

186 subducted Neo-Tethyan crust was older than 40 Ma during the Paleocene/Eocene, it was ascribed
187 a carbonate content of 0.2 wt% (**Alt and Teagle, 1999**). For pelagic sediments, we adopted a
188 carbonate content of typical deep-sea carbonate oozes (90 wt%) (**Kroenke et al., 1991**), an
189 organic carbon content of 1 wt%, a thickness of 200 m, and a density of 1.9 t/m^3 , similar to
190 uncompact deep-sea deposits (**Sykes, 1996**). These values are close to those used by **Edmond**
191 **and Huh (2003)** and **Johnston et al. (2011)** ($\text{CaCO}_3 = 100 \text{ wt\%}$; thickness = 200 m). They can
192 also be compared to those calculated from the model of **Kent and Muttoni (2013)** ($\text{CaCO}_3 =$
193 100 wt\% ; thickness of ~240-270 m from 65 to 50 Ma), who explicitly computed sediment
194 thickness as a function of pelagic carbonate productivity and the timing of residence of the
195 oceanic crust in the Neo-Tethyan equatorial belt zone. Note that sediment thickness may have
196 been locally higher due to the presence of submarine fans or margin deposits such as carbonate
197 platforms. However, paleogeographic reconstructions indicate that north of Greater India, the
198 Paleocene-Eocene Neo-Tethys ocean was deep (**Heine et al., 2004**), favoring the predominance
199 of pelagic deposition. For Arabia and Africa, the same conclusion can be drawn from
200 palinspastic reconstructions of **Barrier and Vrielynck (2008)**, who showed that only a small
201 proportion of margin sediments were subducted during the Paleocene and the Eocene, compared
202 to deep sediments.

203

204 3.2.2. Continental crust and Indian margin sediments

205 For subduction of northern Greater Indian passive margin sediments, a simplified passive
206 continental margin geometry consisting of a sedimentary succession overlying the basement was
207 designed (**Figure 2**). Basement-sediment and the upper sediment interfaces were modeled using
208 sigmoidal functions. Their shape was inspired from the geometry of the North American Atlantic

209 passive margin (**Watts and Thorne, 1984**), which may have been a modern analogue to the pre-
210 collisional northern-Indian passive margin (**Brookfield, 1993**). Total length of the margin
211 sediment succession was set to 600 km, following **Brookfield (1993)** and in agreement with
212 back-stripping reconstructions of **Liu and Einsele (1994)** and **Guillot et al. (2008)**. Maximum
213 sediment thickness was set to a mean value of 4 km (uncompacted), based on recent estimations
214 of syn-rift/post-rift Neo-Tethyan margin sediment thicknesses of **Sciunnach and Garzanti**
215 **(2012)**. Although the lithology of the margin was variable, the proportion of carbonate sediments
216 and organic matter may have been important (**Beck et al., 1995; Liu and Einsele, 1994;**
217 **Sciunnach and Garzanti, 2012**). Average contents of 50 wt% and 1 wt% were chosen for
218 carbonate and organic carbon content, respectively. Uncompacted margin sediments were given
219 a density of 2 t/m³ as calculated from data of **Sciunnach and Garzanti (2012)**.

220

221 **3.3. Decarbonation efficiency of subducted materials**

222 3.3.1. Oceanic crust and pelagic sediments

223 In the "carbonate subduction factory" model, CO₂ produced during oceanic subduction
224 processes originates from deep metamorphic decarbonation of subducted crust and sediments
225 (carbonate and organic matter), and is assumed to be released at volcanic arcs following partial
226 melting of the subducting oceanic crust and metasomatism of the overlying mantle (**Hilton et al.,**
227 **2002; Gorman et al., 2006**). This common statement was followed in the CSFM model (**Figure**
228 **3**), therefore ignoring possible additional CO₂ sources, in particular decarbonation of the
229 overlying crust (**Lee et al., 2013**). The amount of CO₂ released through arc volcanism was
230 calculated as follows: first, for each time step, the total volume of subducting sediment and crust
231 was computed. We assumed this volume to be similar to that encompassing metamorphic carbon

232 loss in the sub-arc zone ($\sim 120 \pm 40$ km depth; **England and Katz, 2010**) (i.e., no variation of
233 volume during the subduction process before decarbonation). Then, the amount of CO₂ emitted
234 at the surface was calculated from arc decarbonation efficiency, defined as the ratio of the
235 volcanic gas CO₂ flux to the input of subducted carbon (e.g., **Johnston et al., 2011**) (**Annex 2**).
236 Decarbonation efficiency values were based on modern decarbonation efficiencies calculated
237 recently by **Johnston et al. (2011)** using a mass balance approach, and those computed by
238 **Gorman et al. (2006)** based on thermodynamic modelling. Decarbonation efficiencies at sub-arc
239 depth of **Johnson et al. (2011)** vary from 0.1 to 70% for ten subduction trenches, with most
240 values ranging between 18 and 54%. They are quite similar to the mean values of **Gorman et al.**
241 **(2006)** ($\sim 16\%$ and $\sim 63\%$, if volcanic CO₂ is derived from decarbonation at sub-arc depth only, or
242 both at fore-arc and sub-arc depths, respectively), which are based on 41 subduction zones. We
243 have retained values of 15 to 60%. Note that such values exceed the one used by **Kent and**
244 **Muttoni (2013)** to perform similar calculations (10%), based on ¹⁰Be data in arc volcanoes of
245 Central America (**Tera et al., 1986**). Finally, the time lag between decarbonation at depth and
246 gas emission at the surface was set to 2 Ma, averaging time scales of **Turner (2002)** (0.4 to 4
247 Ma).

248

249 3.3.2. Continental crust and Indian margin sediments

250 Due to the lack of aqueous fluids in continental crust, continental subduction zones are
251 expected to be devoid of significant syn-subduction arc volcanism in the overlying plate (**Zheng,**
252 **2012**). Although volcanism may have continued in Tibet after 50 Ma (**Ji et al., 2009; Rohrmann**
253 **et al., 2012**), in the model oceanic slab-related metamorphic decarbonation and magma
254 generation was considered to last until the arrival of the continental lithosphere at sub-arc depth

255 (i.e., 80 km) (**Figure 3**) Using preferred geometric parameters of **Leech et al. (2005)** for
256 subduction of the Indian plate, this depth is reached ~1.5 to 2 Ma after the initiation of
257 continental subduction. Despite cessation of volcanic activity, subduction of continental margin
258 sediments may have been associated to active CO₂ degassing at springs or vents as a result of
259 efficient metamorphic sediment decarbonation at T > 300°C (e.g., **Becker et al., 2008; Evans et**
260 **al., 2008**). **Kerrick and Caldeira (1993)** suggested that limited collision-related prograde
261 metamorphism of marly lithologies may induce a CO₂ loss of ~10 wt%, equivalent to a
262 decarbonation efficiency of ~50% for sediments with a carbonate content of 50 wt% (= 22 wt%
263 CO₂). This value may represent an upper estimate as shown by thermodynamic modeling of
264 **Massonne (2010)**. Above-mentioned studies focus on collision rather than continental
265 subduction, for which to our knowledge no estimations of CO₂ outgassing fluxes or
266 decarbonation efficiency are available. To avoid overestimations of CO₂ production, we assumed
267 that only limited margin sediment decarbonation may have occurred after the onset of
268 continental subduction at low-grade conditions, with a 1 to 10 wt% efficiency. Time necessary
269 for subducted margin material to reach the 300°C isotherm after the onset of continental
270 subduction at ~55-50 Ma (corresponding to 25 km depth with a normal-subduction geothermal
271 gradient of 15°C/km) was set to 0.5 Ma, as calculated with parameters of **Leech et al. (2005)**.
272 Circulation of CO₂-rich fluids along large-scale collision-related thrust detachments has been
273 proposed as an efficient way to promote degassing at the surface (e.g., **Kerrick and Caldeira,**
274 **1993; Becker et al., 2008**). Following **Skelton (2011)**, who suggested that gas produced during
275 low-grade metamorphism may be rapidly released to the surface (~4000 yr), we considered
276 immediate release of CO₂ to the atmosphere (**Annex 2**).
277

278 **3.4. Results**

279 3.4.1. Tethyan subduction rate

280 During the Paleocene (65 to 56 Ma), the mean subduction rate (i.e., all plates) has a
281 constant value of ≈ 5.5 cm/yr (**Figure 4A**). Increased rates (up to 8.3 cm/yr) are computed
282 between 56 and 53 Ma, before a gradual decrease to 3 cm/yr at 35 Ma. India-Asia convergence,
283 which reaches up to 16.7 cm/yr at 53-52 Ma, exerts the main control on high early Cenozoic
284 subduction rates.

285

286 3.4.2. Greenhouse gas production

287 It is important to note that decarbonation efficiencies may have strongly varied with time,
288 depending particularly on the plate age and sediment thickness (**Peacock, 2003; Connolly, 2005;**
289 **Johnston et al., 2011**). However, according to **Johnston et al. (2011)** the decarbonation
290 efficiency is only roughly correlated with convergence (subduction) rate. Therefore, excess CO₂
291 fluxes calculated at minimum (15%) and maximum (60%) efficiencies correspond to extreme
292 scenarios that very likely encompass true excess CO₂ fluxes related to Neo-Tethys closure.

293

294 *3.4.2.1 Without Indian continental subduction*

295 If Greater Indian continental subduction collision is not considered, CO₂ production
296 varies from $0.3\text{-}1.1 \times 10^{18}$ to $0.4\text{-}1.65 \times 10^{18}$ molCO₂/Ma (15%-60% efficiency, respectively)
297 between 65 and 50 Ma (**Figure 4B**). This amounts up to 37% of the modern global outgassing
298 rate ($\sim 4\text{-}10 \times 10^{18}$ molCO₂/Ma; **Berner, 2004**). Highest possible values occur at a peak centered
299 on the EECO (54-51 Ma). These flow rates exceed those computed before 65 Ma and after 50
300 Ma. If subduction of the Indian plate alone was acting as the main driver of CO₂ degassing, as

301 proposed by **Kent and Muttoni (2008)**, maximal CO₂ production would reach 1.1×10^{18}
302 molCO₂/Ma from 54 to 50 Ma (**Figure 4C**), corresponding to 11-27% of the modern outgassing
303 rate.

304

305 *3.4.2.2. With Indian continental subduction*

306 Decarbonation of Greater Indian margin sediments, added to the last volumes of pelagic
307 sediments at sub-arc depth, results in a peak of CO₂ production ~2 Ma after the onset of
308 continental subduction, considering a constant decarbonation efficiency (**Figure 4D**). In our
309 model, continental subduction must start at 52.5 Ma (consistent for example with stratigraphic
310 arguments of **Najman et al., 2010** and paleomagnetic arguments of **Huang et al., 2015b**) for
311 maximum CO₂ emissions to occur at ~51 Ma, i.e. coeval to maximum recorded temperatures
312 during the EECO (**Zachos et al., 2008**). In this case, CO₂ degassing flow rates are in the range
313 $0.6-3.35 \times 10^{18}$ molCO₂/Ma (1/15%-10/60% efficiencies for margin/pelagic sediments,
314 respectively), corresponding to 6%-84% of the modern CO₂ outgassing rate. A 55 Ma age for the
315 inset of continental subduction results in even higher production ($0.65-3.7 \times 10^{18}$ molCO₂/Ma)
316 although on a peak centered at 53.5 Ma, ~2 Ma before maximum recorded paleotemperatures
317 (**Figure 4D**). In contrast, late subduction (50 Ma) results in the presence of two smaller peaks:
318 the first one (54-52 Ma) only relates to decarbonation of subducted pelagic sediments whereas
319 the second (48-46 Ma) largely results from decarbonation of margin sediments ($0.32-2 \times 10^{18}$
320 molCO₂/Ma for 1%-10% efficiency, respectively) (**Figure 4D**). If the Indian plate alone is
321 considered (52.5 Ma), CO₂ production reaches $0.46-3 \times 10^{18}$ molCO₂/Ma (1/15%-10/60%
322 efficiencies for margin/pelagic sediments, respectively) at ~52-51 Ma, amounting up to 75% of
323 the modern outgassing rate (**Figure 4E**).

324

325 **4. MODELING THE IMPACT OF NEOTHETYS CLOSURE**

326 To test the influence of calculated excess CO₂ fluxes on Paleocene/Early Eocene climate,
327 we carried out simulations using the GEOCLIM model (**Donnadieu et al., 2004; Godd ris et**
328 **al., 2008**). This model couples a 3-D General Circulation model (GCM) called FOAM (**Jacob,**
329 **1997**) to a box model of geological carbon-alkalinity cycles called COMBINE (**Godd ris and**
330 **Joachimski, 2004**). The GCM FOAM is used in mixed-layer mode, where atmosphere is linked
331 to a 50-meter mixed-layer ocean, which parameterizes heat transport through diffusion, in order
332 to reduce computation time (one GEOCLIM simulation needs up to 12 GCM simulations). This
333 GCM is forced by a large range of *p*CO₂ (200 up to 4200 ppmv) to generate an offline catalogue
334 of continental air temperature and continental runoff with a spatial resolution of 7.5° long × 4.5°
335 lat. For each corresponding atmospheric *p*CO₂ value, the GEOCLIM model calculates the
336 temperature and the runoff of each grid cell through a linear interpolation procedure from the
337 climatic catalogue. This procedure is repeated until a steady-state is reached that corresponds to a
338 stable atmospheric CO₂ and temperature. The model uses an ocean geometry divided into two
339 polar oceans (including a photic zone and a deep ocean reservoir), a low- to mid-latitude ocean
340 (including a photic zone, a thermocline and a deep ocean reservoir), two epicontinental seas
341 (both with a photic zone and a deep epicontinental reservoir) and the atmosphere. A full
342 description of GEOCLIM and its components COMBINE and FOAM can be found in **Godd ris**
343 **and Joachimski (2004)** and **Donnadieu et al. (2006)**.

344

345 **4. 1 GEOCLIM simulations**

346 We first calculated the steady-state $p\text{CO}_2$, assuming that the total CO_2 consumed by
347 continental silicate rocks weathering equals the total solid Earth CO_2 degassing flux (**Walker et**
348 **al., 1981**). Due to the non-consensus about the Earth degassing rate for the last 200 Ma, the
349 degassing flux was assumed constant and fixed at a modern value of 6.8×10^{18} mol CO_2 /Ma,
350 which is required in the model to balance the global consumption through the weathering of
351 silicate lithologies (**Donnadieu et al., 2006**). Each terrestrial grid was prescribed a similar
352 lithology, in which basalt weathering reaches a 30% contribution of the total silicate weathering
353 flux taken at present day (**Dessert et al., 2003**) (similar to UNI configuration of **Lefebvre et al.**
354 **(2013)**). **Lefebvre et al. (2013)** have shown that with this configuration steady-state $p\text{CO}_2$ is
355 similar at 65, 52 and 30 Ma (320-350 ppm), despite variations in paleogeography. An Early
356 Eocene (52 Ma) paleogeographic reconstruction was thus used in the simulation, which runs
357 from 65 Ma to 40 Ma. Land-ocean configuration was built from a synthesis of paleomagnetic
358 data and geologic constraints (**Besse and Courtillot, 2002; Dercourt et al., 1993**). Obliquity
359 and radiation solar constant were assumed to equal present-day values.

360 The main geological forcing tested in the simulation is the additional CO_2 fluxes
361 calculated from CFSM. CO_2 fluxes of **Kent and Muttoni (2013)** have also been tested, using
362 decarbonation efficiencies of 15% and 60% in addition to the original value of 10% proposed by
363 the authors. Computed CO_2 outgassing rates resulting from Neo-Tethys closure were integrated
364 to GEOCLIM, in an age step of 1 Ma.

365

366 4.2. $p\text{CO}_2$ evolution during the LPEE and the EECO

367 If minimum decarbonation efficiency (15%) is considered, $p\text{CO}_2$ increase following
368 excess CO_2 flux is negligible (**Figure 5C**). For example, the addition of continental subduction,

369 which results in higher CO₂ fluxes, allows reaching maximum *p*CO₂ of only 360-365 ppm at 51
370 Ma (i.e. close to steady state values).

371 If maximum decarbonation efficiency (60%) is considered, calculated excess CO₂ fluxes
372 lead to *p*CO₂ of 430-450 ppm from 65 to 54 Ma (**Figure 5C**). Without continental subduction,
373 between 54 and 51 Ma, *p*CO₂ increases up to 500-550 ppm. It then decreases to steady state
374 *p*CO₂ values from 48 Ma. With continental subduction, *p*CO₂ can reach much higher values. In
375 the preferred scenario (initiation of continental subduction at 52.5 Ma), *p*CO₂ strongly increases
376 at 54 Ma up to reach a peak of ~770 ppm at 51.5 Ma. It then decreases to values close to steady
377 state at 47 Ma (**Figure 5C**). If continental subduction begins at 55 Ma, a peak of similar
378 amplitude (770 ppm) occurs at 53 Ma (**Figure 5D**). In contrast, a 50 Ma age for the initiation of
379 subduction results in two peaks of smaller amplitude, with *p*CO₂ values of ~520 and ~570 ppm at
380 ~52 and 48 Ma, respectively (**Figure 5D**).

381 Using excess CO₂ fluxes of **Kent and Muttoni (2013)** leads to low atmospheric CO₂
382 concentrations whatever chosen decarbonation efficiencies (10, 15 or 60%) (**Figure 5E**).
383 Following an increasing trend of excess CO₂ flux, *p*CO₂ progressively increases from 330-340-
384 445 ppm at 65 to 335-345-475 ppm at 50 Ma (10%-15%-60% efficiency, respectively). It then
385 decreases rapidly decreases to values lower than 335 ppm after 48 Ma.

386

387 **5. DISCUSSION**

388

389 5.1. Impact of Neo-Tethys closure on Paleocene/Eocene climate

390 It has long been suggested that Paleocene/Eocene warming was not due to an increase of
391 mantle degassing, calling for additional sources of atmospheric CO₂ (**Engebretson et al. 1992**;

392 **Kerrick and Caldeira, 1993; Hilting et al., 2008; Van der Meer et al., 2014). Kerrick and**
393 **Caldeira (1993)** first showed, on the basis of a simple carbon cycle model that the minimal
394 value of additional CO₂ necessary to drive climate warming during the LPEE and the EECO (≥
395 1°C) may have been close to ~10¹⁸ molCO₂/Ma. More recently, **Lefebvre et al (2013)** used the
396 GEOCLIM model to calculate that a higher flux of ~3.4x10¹⁸ molCO₂/Ma, corresponding to a
397 50% increase of global CO₂ degassing rate, was needed to reach a *p*CO₂ value of 930 ppm
398 consistent with geochemical proxies compiled by **Beerling and Royer (2011)**.

399 Estimations of CO₂ outgassing resulting from Neo-Tethys closure during the Cretaceous
400 and the Paleogene have been previously proposed by **Edmond and Huh (2003), Johnston et al.**
401 **(2011)** and **Kent and Muttoni (2013)**. Values calculated from data of **Kent and Muttoni (2013)**
402 (< 1.3x10¹⁷ molCO₂/Ma from 80 to 50 Ma) fall largely below those required by modeling of
403 **Lefebvre et al. (2013)** to reach estimated *p*CO₂, largely because of their choice of limited
404 decarbonation efficiency during subduction (10%). In contrast, estimations of **Edmond and Huh**
405 **(2003)** and **Johnston et al. (2011)** vary from 0.5 to 4x10¹⁸ molCO₂/Ma for the entire Tethyan
406 arc. According to results of **Lefebvre et al. (2013)**, the higher range of these values should allow
407 to sustain a warm climate during the Paleocene and the lower Eocene. However, excess CO₂ flux
408 calculations of **Edmond and Huh (2003)** and **Johnston et al. (2011)** represent only average
409 values based on simple assumptions such as a constant subduction rate for the entire Upper
410 Cretaceous-Lower Cenozoic. Nevertheless, these estimates are generally higher than those
411 calculated using CFSM. We rather suggest that between 65 and ~55 Ma (i.e., before the oldest
412 possible age of Indian continental subduction), Neo-Tethys closure may have released less than
413 ~10¹⁸ molCO₂/Ma, in particular owing to subduction rates lower than the one used by **Edmond**
414 **and Huh (2003)** and **Johnston et al. (2011)** (~5.5 versus 8 cm/yr, respectively). Using the

415 GEOCLIM model, CO₂ outgassing values obtained with maximum decarbonation efficiency
416 (60%) allow to reach a *p*CO₂ of ~430 ppm, which is in agreement with proxies for the Early
417 Paleocene (65-60 Ma) (**Beerling and Royer, 2011**) (**Figure 5C**). Therefore, our modeling
418 suggests that high decarbonation efficiency was a prerequisite for the "carbonate subduction
419 factory" to have a significant impact on global climate at that time. In addition, GEOCLIM
420 seems unable to explain the onset of Paleocene/Eocene warming at 58 Ma, coevally to an
421 increase of atmospheric *p*CO₂ (**Beerling and Royer, 2011**) (**Figure 5A, B, C**). Similar
422 conclusions can be drawn from climatic simulations performed with excess CO₂ fluxes of **Kent**
423 **and Muttoni (2013)**, even using a decarbonation efficiency of 60% (**Figure 5E**). In that case,
424 *p*CO₂ only steadily increases during the Paleocene and remains lower than values suggested by
425 proxies (**Figure 5C**).

426 A more significant contribution of Neo-Tethyan closure to global warming may have occurred
427 close to the EECO (~52-49 Ma), owing in particular to an increase of the Indian subduction rate
428 (**Figure 4A**). This contribution is also conditioned by maximum decarbonation efficiency, and
429 by the onset of Indian continental subduction at ~52 Ma. With these two conditions fulfilled, the
430 model allows to reach *p*CO₂ values lower than, but close to proxy ones (< 850 ppm versus ~1000
431 ppm, respectively) (**Figure 5B**). Based on calculations of climate sensitivity to atmospheric CO₂
432 of GEOCLIM performed by **Godderis et al (2014)** (2.4°C for a *p*CO₂ doubling at 52 Ma), they
433 may have resulted in a related global atmospheric temperature increase of ~2°C compared to the
434 Paleocene. In contrast, if India-Asia continental subduction occurred much later (i.e., equivalent
435 to no collision), Neo-Tethys contribution to the EECO remained negligible, even with a
436 decarbonation efficiency of 60% (**Figure 5C**). Calculations performed with input data of **Kent**
437 **and Muttoni (2013)** lead to the same interpretation for the Early Eocene (**Figure 5E**).

438 Finally, our study allows to clearly moderate the impact of the Neo-Tethyan "carbonate
439 subduction factory" on Paleocene/Eocene greenhouse, at odds with **Edmond and Huh (2003)**,
440 **Johnston et al. (2011)** and **Kent and Muttoni (2008)**, but in accordance with recent conclusions
441 of **Kent and Muttoni (2013)** and **Lee et al. (2013)**. As a consequence, the strong decrease of
442 CO₂ production after India-Asia collision was not a driver of pCO₂ decrease and global cooling
443 recorded after the late Eocene (**Kent and Muttoni, 2013**).

444

445 5.2 Potential additional sources of atmospheric carbon dioxide

446 5.2.1. Large Igneous Provinces

447 Since the role of Neo-Tethys closure on the onset of the LPEE and the EECO likely has
448 been limited, other sources of excess greenhouse gases should be called for. These should ideally
449 explain the decrease of marine and terrestrial $\delta^{13}\text{C}$ during the LPEE, and its slight increase
450 during the EECO (**Zachos et al. 2001**) (**Figure 5A**). Numerous geological explanations have
451 been previously postulated for the entire early Cenozoic greenhouse, among which a flare up in
452 the activity of igneous provinces is the most common (e.g., **Eldhom and Thomas, 1993**;
453 **Reagan et al. 2013**). **Reagan et al. (2013)** presented a review of Late Paleocene to Early Eocene
454 magmatism, characterized by the significant activity of at least three major igneous provinces:
455 the North Atlantic Igneous Province, the Siletzia terrane of the northwestern United States and
456 the Yakutat block in southern Alaska. Added to enhanced activity of Neo-Tethys and eastern
457 Pacific subduction-related volcanism, **Reagan et al. (2013)** concluded for an overall excess CO₂
458 production of $\sim 2.3 \times 10^{18}$ molCO₂ for the late Paleocene-Early Eocene period. Even though this
459 value may appear important, it encompasses time duration of several million years. Assuming a
460 10 Ma duration for significant magmatism (see **Reagan et al. (2013)**, Figure 6), the calculated

461 excess CO₂ flow rate falls to only $\sim 2.3 \times 10^{17}$ molCO₂/Ma on average, one order of magnitude
462 below fluxes necessary to reach a *p*CO₂ comparable to proxies using the GEOCLIM model. This
463 value can be compared to that of **Eldholm and Thomas (1993)**, who calculated that more than
464 2.3×10^{18} molCO₂ may have been released to the atmosphere by the NAIP only, from 58 to 52
465 Ma (revised to 61-53 Ma by **Menzies et al. (2002)**), corresponding to a flux of $\sim 3 \times 10^{17}$
466 molCO₂/Ma. We infer, on the base of GEOCLIM modeling, that the effect of enhanced
467 magmatic activity on LPEE warming and the EECO may also have been limited, unless related
468 fluxes have been severely underestimated in the literature. As discussed later, this conclusion is
469 consistent with previous studies of carbon cycle dynamics during the early Cenozoic (**e.g.,**
470 **Hilting et al., 2008; Komar et al., 2013**).

471

472 5.2.2. Metamorphic decarbonation

473 **Lee et al. (2013)** argued that the decarbonation of platform carbonates stored on the
474 continental upper plate during subduction-related magmatism may have been far more efficient
475 in driving early Cenozoic greenhouse than the activity of igneous provinces or of the "subduction
476 factory". **Lee et al. (2013)** calculated that global CO₂ degassing could have reached 3.7-5.5 times
477 the present day value from during from ~ 140 Ma to 50 Ma, making $2.2-3.7 \times 10^{19}$ molCO₂/Ma for
478 a present day value of 6.8×10^{18} molCO₂/Ma (as calculated with GEOCLIM). Cooling initiation
479 during the late Eocene would then have resulted from a transition from a continental-dominated
480 to an island arc-dominated world ca. 52 Ma. The EECO would represent a "last spurt of CO₂
481 production associated with an Eocene magmatic flare-up in western North America", based on
482 previous work of **Nesbitt et al. (1995)** and **Kerrick and Caldeira (1998)**. In light of the
483 GEOCLIM model, we argue that CO₂ fluxes of **Lee et al. (2013)** are clearly overestimated for

484 the EECO, as $p\text{CO}_2$ close to proxies would be obtained for excess fluxes lower by approximately
485 one order of magnitude. If they are applied to the EECO, fluxes calculated by **Kerrick and**
486 **Caldeira (1998)** for the 60-55 Ma period (3×10^{18} mol CO_2/Ma) seem more reasonable. Similar to
487 the decarbonation of pelagic carbonate sediments, crustal decarbonation related to magmatic or
488 metamorphic events should lead to a positive shift of exogenic $\delta^{13}\text{C}$ (**Lee et al., 2013**), in
489 agreement with proxies for the EECO. In contrast, the LPEE was characterized by a related
490 negative shift in $\delta^{13}\text{C}$ (**Zachos et al., 2001**), suggesting additional or alternate sources of excess
491 isotopically-light CO_2 .

492

493 5.2.3 Organic carbon sources

494 Several authors have thus proposed organic carbon (C_{org}) to be a significant source of
495 excess CO_2 during the LPEE and / or the EECO, mostly based on carbon cycle models (e.g.,
496 **Beck et al., 1995; Kurtz et al., 2003; Hilton et al., 2008; Kroeger and Funnel, 2012; Komar**
497 **et al., 2013**). The importance of organic carbon dynamics was clearly highlighted by **Hilting et**
498 **al. (2008)**, who used a carbon cycle model tuned with marine $\delta^{13}\text{C}$ data to calculate Paleocene
499 and Eocene $p\text{CO}_2$ values. These authors managed to reproduce $p\text{CO}_2$ values globally consistent
500 with observations, even though background volcanic / metamorphic CO_2 degassing was kept
501 constant. According to their simulation, large changes in $p\text{CO}_2$ (and thus, temperature) may
502 occur independently of the endogenic carbon cycle. Similar conclusions were drawn by **Komar**
503 **et al. (2013)** on the basis of coupled LOSCAR-GEOCARB carbon cycle modeling. They showed
504 that a mantellic source of excess CO_2 during the LPEE would have led to a deepening of the
505 CCD much more important than evidenced from observations. Although based on a different
506 approach, this conclusion is in good accordance with our suggestion of a moderate impact of

507 LIPs on the LPEE (and the EECO). Instead, **Komar et al. (2013)** proposed that perturbations of
508 the carbon cycle observed during the LPEE were likely controlled by decrease of net organic
509 carbon burial, either through increased C_{org} oxidation, or through decreased C_{org} burial. Suitable
510 sources of organic carbon to the exogenic system include methane hydrates, which may have
511 accumulated in marine sediments during the early Paleocene, and collapsed during the LPEE
512 (**Komar et al., 2013**), terrestrial organic matter previously accumulated in swamps (**Kurtz et al.,**
513 **2003**), or important reservoir petroleum generation (**Kroeger and Funnel, 2012**). However, the
514 timing of maximum hydrocarbon production calculated by **Kroeger and Funnel (2012)** likely
515 occurred during the EECO, which is hardly reconcilable with coeval increase in marine $\delta^{13}\text{C}$
516 unless net C_{org} burial was significantly higher than during the LPEE (e.g., **Kurtz et al., 2003**).
517 Finally, **Beck et al. (1995)** postulated that Neo-Tethyan marine organic matter accumulated on
518 Eurasian and Greater Indian margins may have been oxidized during India-Asia collision and
519 subsequent exhumation, provided collision occurred no later than ~ 60 Ma. About 1.6×10^{18}
520 molC/Ma may have been released during the first 4 Ma of the LPEE, enough to explain the
521 concurrent negative shift in $\delta^{13}\text{C}$. Using our model, we calculate that the organic carbon
522 contained within Greater Indian margin alone ($\sim 3.8 \times 10^6 \text{ km}^3$) amounts $\sim 8 \times 10^{18}$ molC (for a
523 sediment organic carbon content of 1 wt%), corresponding to a flux of $\sim 2 \times 10^{18}$ molC/Ma (i.e.,
524 close to estimates of **Beck et al. (1995)**) if all C_{org} was oxidized during exhumation. This was
525 probably not the case, and our estimate is likely overestimated. Nevertheless, it shows that
526 oxidation of Neo-Tethyan marine C_{org} may have contributed to the LPEE if collision occurred
527 earlier than assumed in our model (e.g., **Hu et al., in press**), to an extent that deserves to be
528 quantified more accurately in future studies.

529 In contrast to the LPEE, the rise in marine $\delta^{13}\text{C}$ from 52.5 to 50 Ma suggests that the
530 EECO was characterized by increased net organic carbon burial (as proposed by **Komar et al.**
531 **(2013)** with the methane hydrate hypothesis), or as we test in this paper, by the addition of
532 excess CO_2 derived from one or several sources with heavier $\delta^{13}\text{C}$ signatures. Both explanations
533 need to be reconciled with recent observations that silicate weathering may have been reduced
534 during the EECO, as discussed below.

535

536 5.3. Are modeled silicate weathering fluxes overestimated for the EECO?

537 Most carbon cycle models agree that during the Early Eocene volcanic degassing alone
538 was insufficient to sustain the high $p\text{CO}_2$ values required by proxies, due to important
539 weathering rates at that time (e.g., **Berner, 2006; Lefebvre et al., 2013; Komar et al., 2013**).
540 For example, **Berner (2006)** found, based on the time evolution of seawater $^{87}\text{Sr}/^{86}\text{Sr}$ that
541 weathering was mainly controlled by increased basaltic alteration, resulting in a $p\text{CO}_2$ of ~ 700
542 ppm at 50 Ma, i.e. lower than observations (~ 1000 ppm). Indeed, decreasing of seawater Sr
543 isotopic signature during the Paleocene and the Early Eocene is consistent with the alteration of
544 igneous provinces such as the Deccan Traps or the NAIP (**Hoddell et al., 2007**). In detail, most
545 paleogeographic reconstructions show that the highly weatherable Deccan traps reached the
546 equatorial humid belt (between 5°S and 5°N), where weathering is maximum, at ~ 55 Ma, with a
547 maximum of area between ~ 50 Ma and ~ 35 Ma (**Dercourt et al., 1993; Besse and Courtillot,**
548 **2002; Van Hinsbergen et al., 2011a, 2012**). Accordingly, taking explicitly into account the
549 impact of paleogeography on the long term carbon cycle as done by the GEOCLIM model has
550 led **Lefebvre et al. (2013)** to suggest that the EECO was characterized by high weathering rates
551 related to weathering of the Deccan traps. As a consequence, the model calculates a very low

552 equilibrium $p\text{CO}_2$ of 340 ppm at that time. Calculations of **Kent and Muttoni (2013)** also
553 pointed to an increase of silicate weathering, and thus of CO_2 consumption during the LPEE and
554 the EECO due to the arrival of Greater India in the equatorial humid belt at that time.

555 Even though most models and reconstructions seem to agree with the hypothesis of
556 increased weathering during the Early Eocene, several proxy-based observations rather suggest
557 that silicate weathering may have been reduced specifically during the EECO. The first one is
558 based on the estimation of the carbonate compensation depth (CCD) during the Paleogene
559 (**Hancock et al., 2007; Leon-Rodriguez and Dickens, 2010; Pälike et al., 2012; Slotnick et**
560 **al., 2014**). During the LPEE, deep-sea carbonate records show a progressive deepening of the
561 CCD that can be attributed to enhanced alkalinity supply to the oceans as a result of enhanced
562 weathering (**Komar et al., 2013**). During the EECO, high $p\text{CO}_2$ values (~ 1000 ppm) similarly
563 should have sustained high silicate weathering and thus favored a deep position of the CCD. In
564 contrast, available records suggest its strong shoaling at that time (**Pälike et al. 2012; Slotnick et**
565 **al., 2014**), which according to **Komar et al. (2013)** hardly conforms to the intense weathering
566 deduced from carbon cycle models. However, previous GEOCLIM modeling showed that a
567 constant silicate weathering flux does not mean a fixed $p\text{CO}_2$ (and thus a fixed CCD), due to the
568 major role played by continental configuration on $p\text{CO}_2$ values (**Donnadieu et al., 2006**). The
569 second observation is based on $\delta^7\text{Li}$ chemistry of Paleocene and Eocene marine sediments,
570 compiled by **Misra and Froelich (2012)**. These authors argued that Li isotopes allow
571 discriminating between periods of high tectonic uplift associated with important physical and
572 chemical weathering, and periods of low alteration (**Froelich and Misra, 2014**). According to
573 **Froelich and Misra (2014)**, the LPEE and the EECO were characterized by slow weathering
574 rates, as shown by a low and constant $\delta^7\text{Li}$ trend. This strong discrepancy with previous

575 interpretations is attributed to the absence of continental reliefs at that time, preventing
576 significant weathering of uplifted, fresh silicate rocks. According to **Froelich and Misra (2014)**,
577 only moderate additional CO₂ may have allowed increasing *p*CO₂ and global temperature up to
578 the end of the EECO. Note that for the LPEE, this interpretation is in contradiction with that of
579 **Komar et al. (2013)** based on the CCD. In addition, recent modeling of **Vigier and Godderis**
580 **(2015)** suggests that the oceanic δ⁷Li record of the Early Eocene could equally be explained by
581 intense soil production rates (i.e, intense chemical weathering). These contradictory observations
582 show that the intensity of silicate weathering during the LPEE and the EECO still suffers from
583 strong uncertainties, as already highlighted by **Kent and Muttoni (2013)**. Additional proxy-
584 based observations are thus needed to calibrate weathering rate values obtained from models,
585 which for example still lack the explicit integration of uplift on carbon cycle evolution (**Lefebvre**
586 **et al., 2013**).

587

588 **6. CONCLUSION**

589 In order to test the role that Neo-Tethys closure may have exerted on warm Paleocene /
590 Early Eocene climate through CO₂ degassing at arc volcanoes, we have calculated the volume of
591 buried pelagic sediments and associated volcanic CO₂ release during the LPEE and the EECO,
592 and its impact on atmospheric *p*CO₂ and atmospheric temperature at that time. To do so, we have
593 applied most recently published convergence rate parameters and decarbonation efficiencies to a
594 simplified Neo-Tethyan geometry, and integrated calculated excess CO₂ fluxes in a state-of-the-
595 art carbon cycle model (GEOCLIM).

596 We show that Neo-Tethys closure was able to bury significant volumes of pelagic
597 sediments at that time. The inset of Indian continental subduction at 55-50 Ma may have

598 potentially given rise to important volumes of excess CO₂, through decarbonation of thick
599 margin sediment accumulations. However, GEOCLIM modeling demonstrates that these
600 volumes do not generally allow reaching *p*CO₂ (and thus temperatures) as high as those inferred
601 from geochemical proxies. Atmospheric CO₂ concentration may have only been able to reach
602 significantly high values during the EECO (up to 770 ppm), but only if decarbonation efficiency
603 was at its maximum at that time. This finding leads us to temper the impact of Neothetys closure
604 on the LPEE and the EECO, calling for additional sources of excess CO₂.

605 Among these, GEOCLIM modeling suggests that in light of available published data, the
606 volume of CO₂ released by Large Igneous Province volcanism was one order of magnitude too
607 low to have had a significant impact on climate during the Paleocene and the Early Eocene.
608 Other recently proposed mechanisms of CO₂ release such as a decrease of net organic carbon
609 burial may have been more efficient in driving Paleocene/Eocene warming.

610 Finally, an alternate explanation may be that CO₂ consumption may have been lower than
611 suggested by carbon cycle models, calling for a better calibration of early Cenozoic weathering
612 rates.

613

614

615 ANNEX 1.

616 For each plate, subduction rates at each time step were corrected for convergence
617 obliquity related to the orientation of the subduction trench using spherical trigonometric
618 equations of the following form:

$$619 \text{Rate}_{corr} = \frac{\tan^{-1}(\tan A \cdot \cos B)}{t_2 - t_1} \quad (1)$$

$$620 \text{with } A = R_E \cdot \cos^{-1}(\sin \varphi_1 \cdot \sin \varphi_2 + \cos(\lambda_1 - \lambda_2) \cdot \cos \varphi_1 \cdot \cos \varphi_2) \quad (2)$$

$$621 \quad B = \tan^{-1} \left(\frac{\sin(\lambda_2 - \lambda_1) \cdot \cos \varphi_2}{\cos \varphi_1 \cdot \sin \varphi_2 - \sin \varphi_1 \cdot \cos \varphi_2 \cdot \cos(\lambda_2 - \lambda_1) - (B_t - 90^\circ)} \right) \quad (3)$$

622 where $Rate_{corr}$ is the corrected rate, (φ_1, λ_1) and (φ_2, λ_2) the Lat/Long decimal coordinates of two
623 successive points, $t_2 - t_1$ the time step (0.5 Ma), R_E the Earth radius (6378.1 km) and B_t the trench
624 bearing. Based on paleogeographic reconstructions of **Barrier and Vrielynck (2008)** and **Agard**
625 **et al. (2011)**, subduction trenches of Africa and Arabia below Eurasia were given constant
626 bearings of 90°E and 135°E, respectively. For India, orthogonal subduction rate was obtained
627 assuming a bearing of 110°E, similar to the present orientation of the Indus-Yarlung Suture Zone
628 between Indian and Asian rocks.

629

630 ANNEX 2

631 For oceanic crust and pelagic sediments, the decarbonation efficiency (defined as number
632 of moles of CO₂ emitted during a given time step of 0.5 Ma), $nCO_2(t)$, is expressed as:

$$633 \quad nCO_2(t) = F_{decarb} \cdot \left(\frac{V_{sed}(t_0) \cdot \rho_{sed} \cdot (k_1 \cdot W_{CaCO_3-sed} + k_2 \cdot W_{Corg}) + k_1 \cdot V_{crust}(t_0) \cdot \rho_{crust} \cdot W_{CaCO_3-crust}}{M_{CO_2}} \right)$$

$$634 \quad (4)$$

635 where $V_{sed}(t_0)$ and $V_{crust}(t_0)$ designate the volume of subducting sediments and crust (km³) for a
636 given time step at $t_0 = t - \text{time-lag}$ (2 Ma), ρ_{sed} and ρ_{crust} their densities (g cm⁻³), W_{CaCO_3-sed} and
637 $W_{CaCO_3-crust}$ their weight fraction of carbonate, W_{corg} the weight fraction of organic carbon in
638 sediments, k_1 and k_2 are conversion unit factors ($k_1 = 4.161 \times 10^{14}$; $k_2 = 3.46 \times 10^{15}$), M_{CO_2} is the
639 molecular weight of CO₂ (44 g mol⁻¹) and F_{decarb} is the decarbonation efficiency, defined as the
640 mass percentage of carbon subducted as sedimentary carbonate, crustal carbonate and organic
641 matter (carbon input), recycled as CO₂. Subducted volumes $V(t_0)$ were calculated as follows:

$$642 \quad V(t_0) = H \cdot \left(\frac{L_{t[Afr]} \times Rate_{[Afr]}(t_0) + L_{t[Arab]} \times Rate_{[Arab]}(t_0) + L_{t[Ind]} \times Rate_{[Ind]}(t_0)}{t_s} \right) \quad (5)$$

643 where, respectively for subducted sediment or crust volumes $V(t_0)$, H is the sediment or crust
 644 thicknesses (km) ; $Lt_{[Afr]}$, $Lt_{[Arab]}$ and $Lt_{[Ind]}$ are the subduction trench lengths of Africa, Arabia
 645 and India (km) and $Rate_{[Afr]}$, $Rate_{[Arab]}$ and $Rate_{[Ind]}$ the orthogonal subduction rates of Africa,
 646 Arabia and India beneath Eurasia at t_0 (km.Ma⁻¹), and t_s is the time step (0.5 Ma in this study).

647 For continental crust and Indian margin sediments, the decarbonation efficiency (defined
 648 as number of moles of CO₂ emitted by subducting Indian continental margin during a given time
 649 step of 0.5 Ma), $nCO_2(t)_{[Ind]}$, was calculated using an expression close to equation (4):

$$650 \quad nCO_2(t)_{[Ind]} = F_{decarb} \cdot \left(\frac{V_{sed}(t_0) \cdot \rho_{sed} \cdot (k_1 \cdot W_{CaCO_3-sed} + k_2 \cdot W_{Corg})}{M_{CO_2}} \right) \quad (6)$$

651 but where $V_{sed}(t_0)$, ρ_{sed} , W_{CaCO_3-sed} , W_{corg} and F_{decarb} have numerical values specific of margin
 652 instead of pelagic sediments. In this case, $t = t_0$ and $V_{sed}(t_0)$ is represented as:

$$653 \quad V_{sed}(t_0) = V_{sed}(t) = H_{sed} \cdot \left(\frac{Lt_{[Ind]} \times Rate_{[Ind]}(t)}{t_s} \right) \quad (7)$$

654

655 ACKNOWLEDGEMENTS

656 F. Behar and T. Parra are thanked for helpful discussions. The manuscript greatly benefited from
 657 reviews of D.V.Kent and J. Martinod. G. Hoareau and B. Bomou benefited from Post-doctoral
 658 grants from INSU- and INEE-CNRS.

659

660 **BIBLIOGRAPHY**

661

662 Agard, P., Omrani, J., Jolivet, L., Whitechurch, H., Vrielynck, B., Spakman, W., Monié, P., Meyer, B., and Wortel,
663 R.: Zagros orogeny: a subduction-dominated process, *Geol. Mag.*, 148, 692–725, 2011.

664 Alt, J. C. and Teagle, D. A. H.: The uptake of carbon during alteration of ocean crust: *Geochim. Cosmochim. Acta*,
665 63, 1527–1535, 1999.

666 Alvarez, W.: Protracted continental collisions argue for continental plates driven by basal traction, *Earth Planet. Sc.*
667 *Lett.*, 296, 434–442, doi:10.1016/j.epsl.2010.05.030, 2010.

668 Barrier, E. and Vrielynck, B.: *Paleotectonic Maps of the Middle East: Middle East Basins Evolution Programme*,
669 CCGM-CGMW, Paris, 2008.

670 Beck, R. A., Burbank, D. W., Sercombe, W. J., Olson, T. L., and Khan, A. M.: Organic carbon exhumation and
671 global warming during the early Himalayan collision, *Geology*, 23, 387–390, doi:10.1130/0091-
672 7613(1995)023<0387:OCEAGW>2.3.CO;2, 1995.

673 Becker, J. A., Bickle, M. J., Galy, A., and Holland, T. J. B., Himalayan metamorphic CO₂ fluxes: quantitative
674 constraints from hydrothermal springs, *Earth Planet. Sc. Lett.*, 265, 616–629, 2008.

675 Beerling, D. J. and Royer, D. L.: Convergent cenozoic CO₂ history, *Nat. Geosci.*, 4, 418–420, 2011.

676 Bellon, H., Maury, R. C., Sutanto, Soeria-Atmadja, R., Cotten, J., and Polvé, M.: 65 m.y.-long magmatic activity in
677 Sumatra (Indonesia), from Paleocene to present, *B. Soc. Geol. Fr.*, 175, 61–72, 2004.

678 Berner, R. A.: *The Phanerozoic Carbon Cycle: CO₂ and O₂*, Oxford University Press, New-York, 150 pp., 2004.

679 Berner, R. A.: Inclusion of weathering of volcanic rocks in the GEOCARBSULF model, *Am. J. Sci.*, 306, 295–302,
680 2006.

681 Besse, J. and Courtillot, V.: Apparent and true polar wander and the geometry of the geomag-
682 netic field over the last 200 Myr, *J. Geophys. Res.*, 107, 2300, doi:10.1029/2000JB000050, 2002.

683 Boyden, J. A., Müller, R. D., Gurnis, M., Torsvik, T. H., Clark, J. A., Turner, M., Ivey-Law, H., Watson, R. J., and
684 Cannon, J. S.: Next-generation plate-tectonic reconstructions using GPLates, in: *Geoinformatics:*
685 *Cyberinfrastructure for the Solid Earth*, edited by: Keller, G. R. and Baru, C., Cambridge University Press,
686 Cambridge, 95–114, 2011

687 Brookfield, M. E.: The Himalayan passive margin from Precambrian to Cretaceous times, *Sediment. Geol.*, 84, 1–

688 35, 1993.

689 Cramer, B. S., Toggweiler, J. R., Wright, J. D., Katz, M. E., and Miller, K. G.: Ocean overturning since the Late
690 Cretaceous: inferences from a new benthic foraminiferal isotope compilation, *Paleoceanography*, 24, PA4216,
691 doi:10.1029/2008PA001683, 2009.

692 Dercourt, J., Ricou, L. E., and Vrielynck, B.: Atlas Tethys Palaeoenvironmental Maps, Gauthier Villars, CGMW,
693 Paris, 307 pp., 14 maps, 1993.

694 Dessert, C., Dupré, B., Gaillardet, J., François, L. M., and Allègre, C. J.: Basalt weathering laws and the impact of
695 basalt weathering on the global carbon cycle, *Chem. Geol.*, 202, 257–273, 2003.

696 Donnadieu, Y., Goddérès, Y., Ramstein, G., Nedelec, A., and Meert, J. G.: A “snowball Earth” climate triggered by
697 continental break-up through changes in runoff, *Nature*, 418, 303–306, 2004.

698 Donnadieu, Y., Goddérès, Y., Pierrehumbert, R., Fluteau, F., and Dromart, G.: Pangea break up and Mesozoic
699 climatic evolution simulated by the GEOCLIM model, *Geochem. Geophys. Geosy.*, 7, Q11019,
700 doi:10.1029/2006GC001278, 2006.

701 Dupont-Nivet, G., Lippert, P., van Hinsbergen, D. J. J., Meijers, M. J. M., and Kapp, P.: Paleolatitude and age of the
702 Indo-Asia collision: paleomagnetic constraints, *Geophys. J. Int.*, 182, 1189–1198, 2010.

703 Edmond, J. M. and Huh, Y.: Non-steady state carbonate recycling and implications for the evolution of atmospheric
704 $p\text{CO}_2$, *Earth Planet. Sc. Lett.*, 216, 125–139, doi:10.1016/S0012-821X(03)00510-7, 2003.

705 Eldholm, O. and Thomas, E.: Environmental impact of volcanic margin formation, *Earth Planet. Sc. Lett.*, 117, 319–
706 329, doi:10.1016/0012-821X(93)90087-P, 1993.

707 Engebretson, D. C., Kelley, K. P., Cashman, H. J., and Richards, M. A.: 180 million years of subduction, *GSA*
708 *Today*, 2, 93–95, 1992.

709 England, P. C. and Katz, R. F.: Melting above the anhydrous solidus controls the location of volcanic arcs, *Nature*,
710 467, 700–703, doi:10.1038/nature09417, 2010.

711 Evans, M. J., Derry, L. A., and France-Lanord, C.: Degassing of metamorphic carbon dioxide from the Nepal
712 Himalaya, *Geochem. Geophys. Geosy.*, 9, Q04021, doi:10.1029/2007GC001796, 2008.

713 Eyuboglu, Y., Santosh, M., Dudas, F. O., Chung, S. L., and Akaryalı, E.: Migrating magmatism in a continental arc:
714 geodynamics of the Eastern Mediterranean revisited, *J. Geodyn.*, 52, 2–15, 2011.

715 Friedrich, O., Norris, R. D., and Erbacher, J.: Evolution of middle to Late Cretaceous oceans – a 55 m.y. record of

716 Earth's temperature and carbon cycle, *Geology*, 40, 107–110, doi:10.1130/G32701.1, 2012.

717 Froelich, F. and Misra, S.: Was the Late Paleocene–Early Eocene hot because Earth was flat? An ocean lithium
718 isotope view of mountain building, continental weathering, carbon dioxide, and Earth's cenozoic climate,
719 *Oceanography*, 27, 36–49, doi:10.5670/oceanog.2014.06, 2014

720 Gaina, C., van Hinsbergen, D. J. J., and Spakman, W.: Tectonic interactions between India and Arabia since the
721 Jurassic reconstructed from marine geophysics, ophiolite geology, and seismic tomography, *Tectonics*, 34,
722 875–906, doi:10.1002/2014TC003780, 2015.

723 Garzanti, E. and Hu, X.: Latest Cretaceous Himalayan tectonics: obduction, collision or Deccan-related uplift?,
724 *Gondwana Res.*, 28, 165–178, 2014.

725 Gnos, E., Immenhauser, A., and Peters, T.: Late Cretaceous/Early Tertiary convergence between the Indian and
726 Arabian plates recorded in ophiolites and related sediments, *Tectonophysics*, 271, 1–20, 1997.

727 Godd ris, Y. and Joachimski, M. M.: Global change in the Late Devonian: modelling the Frasnian–Famennian
728 short-term carbon isotope excursions, *Palaeogeogr. Palaeoclimatol.*, 202, 309–329, 2004.

729 Godd ris, Y., Donnadi u, Y., Tombozafy, M., and Dessert, C.: Shield effect on continental weathering: implication
730 for climatic evolution of the Earth at the geological time-scale, *Geoderma*, 145, 439–448, 2008.

731 Godd ris, Y., Donnadi u, Y., Le Hir, G., Lefebvre, V., and Nardin, E.: The role of palaeogeography in the
732 Phanerozoic history of atmospheric CO₂ and climate, *Earth-Sci. Rev.*, 128, 122–138, 2014.

733 Gorman, P. J., Kerrick, D. M., and Connolly, J. A. D.: Modeling open system metamorphic decarbonation of
734 subducting slabs, *Geochem. Geophys. Geosyst.*, 7, Q04007, doi:10.1029/2005GC001125, 2006.

735 Guillot, S., Maheo, G., de Sigoyer, J., Hattori, K. H., and Pecher, A.: Tethyan and Indian subduction viewed from
736 the Himalayan high- to ultrahigh-pressure metamorphic rocks, *Tectonophysics*, 451, 225–241, 2008.

737 Hall, R.: Late Jurassic–Cenozoic reconstructions of the Indonesian region and the Indian Ocean, *Tectonophysics*,
738 570–571, 1–41, doi:10.1016/j.tecto.2012.04.021, 2012.

739 Hancock, H. J. L., Dickens, G. R., Thomas, E., and Blake, K. L.: Reappraisal of early Paleogene CCD curves:
740 foraminiferal assemblages and stable carbon isotopes across the carbonate facies of Perth Abyssal Plain, *Int. J.*
741 *Earth Sci.*, 96, 925–946, doi:10.1007/s00531-006-0144-0, 2007.

742 H bert, R., Bezard, R., Guilmette, C., Dostal, J., Wang, C. S., and Liu, Z. F.: The Yarlung Zangbo Ophiolites from
743 Nanga Parbat to Namche Barwa syntaxes, Southern Tibet: a synthesis of petrology, geochemistry and ages with

744 incidences on geodynamic reconstructions of the Neo-Tethys, in: Plate Tectonics of Asia: Geological and
745 Geophysical Constraints, edited by: Zhao, X. X., Xiao, W. J., Wang, C. S., and Hébert, R., *Gondwana Res.*,
746 22, 377–397, 2012.

747 Heine, C., Müller, R.D., Gaina, C., Clift, P., Kuhnt, W., Wang, P., and Hayes, D.: Reconstructing the lost eastern
748 Tethys Ocean Basin: Convergence history of the SE Asian margin and marine gateways: Geophysical
749 Monograph, v. 149, p. 37–54, 10.1029/149GM03, 2004.

750 Hilting, A. K., Kump, L. R., and Bralower, T. J.: Variations in the oceanic vertical carbon isotope gradient and their
751 implications for the Paleocene-Eocene biological pump, *Paleoceanography*, 23, PA3222,
752 doi:10.1029/2007PA001458, 2008.

753 Hilton, D. R., Fischer, T. P., and Marty, B.: Noble gases and volatile recycling at subduction zones, in: Noble Gases
754 in Cosmochemistry and Geochemistry, edited by: Porcelli, D., Ballentine, C. J., and Wieler, R., Mineralogical
755 Society of America, Washington, D.C., 319–370, 2002.

756 Hodell, D. A., Kamenov, G. D., Hathorne, E. C., Zachos, J. C., Röhl, U., and Westerhold, T.: Variations in the
757 strontium isotope composition of seawater during the Paleocene and early Eocene from ODP Leg 208 (Walvis
758 Ridge), *Geochem. Geophys. Geos.*, 8, Q09001, doi:10.1029/2007GC001607, 2007.

759 Hu, X., Wang, J., BouDagher-Fadel, M., Garzanti, E., An, W.: New insights into the timing of the India–Asia
760 collision from the Paleogene Quxia and Jialazi formations of the Xigaze forearc basin, South Tibet, *Gondwana
761 Res.*, doi:10.1016/j.gr.2015.02.007, in press.

762 Huang, W., van Hinsbergen, D. J. J., Maffione, M., Orme, D., Dupont-Nivet, G., Guilmette, C., Ding, L., Guo, Z.,
763 and Kapp, P.: Lower Cretaceous Xigaze ophiolites formed in the Gangdese forearc: evidence from
764 paleomagnetism, sediment provenance, and stratigraphy, *Earth Planet. Sc. Lett.*, 415, 142–153, 2015a.

765 Huang, W., van Hinsbergen, D. J. J., Lippert, P. C., Guo, Z., Dupont-Nivet, G., and Kapp, P.: Paleomagnetic tests of
766 tectonic reconstructions of the India–Asia collision zone, *Geophys. Res. Lett.*, 42, 2642–2649,
767 doi:10.1002/2015GL063749, 2015b.

768 Jacob, R.: Low Frequency Variability in a Simulated Atmosphere Ocean System, PhD thesis, University of
769 Wisconsin, Madison, USA, 1997.

770 Ji, W.-Q., Wu, F.-Y., Chung, S.-L., Li, J.-X., and Liu, C.-Z.: Zircon U-Pb geochronology and Hf isotopic constraints
771 on petrogenesis of the Gangdese batholith, southern Tibet, *Chem. Geol.*, 262, 229–245,

772 doi:10.1016/j.chemgeo.2009.01.020, 2009.

773 Johnston, K. B. F., Turchyn, A. V., and Edmonds, M.: Decarbonation efficiency in subduction zones: implications
774 for warm Cretaceous climates, *Earth Planet. Sc. Lett.*, 303, 143–152, doi:10.1016/j.epsl.2010.12.049, 2011.

775 Kazmin, V. G.: Collision and rifting in the Tethys Ocean: geodynamic implications, *Tectonophysics*, 123, 371–384,
776 1991.

777 Kent, D. V. and Muttoni, G.: Equatorial convergence of India and early Cenozoic climate trends, *P. Natl. Acad. Sci.*
778 *USA*, 105, 16065–16070, doi:10.1073/pnas.0805382105, 2008.

779 Kent, D. V. and Muttoni, G.: Modulation of Late Cretaceous and Cenozoic climate by variable drawdown of
780 atmospheric $p\text{CO}_2$ from weathering of basaltic provinces on continents drifting through the equatorial humid
781 belt, *Clim. Past*, 9, 525–546, doi:10.5194/cp-9-525-2013, 2013.

782 Kerrick, D. M. and Caldeira, K.: Paleatmospheric consequences of CO_2 released during early Cenozoic regional
783 metamorphism in the Tethyan orogeny, *Chem. Geol.*, 108, 201–230, doi:10.1016/0009-2541(93)90325-D,
784 1993.

785 Kerrick, D. M. and Caldeira, K.: Metamorphic CO_2 degassing from orogenic belts, *Chem. Geol.*, 145, 213–232,
786 doi:10.1016/S0009-2541(97)00144-7, 1998.

787 Komar, N., Zeebe, R. E., and Dickens, G. R.: Understanding long-term carbon cycle trends: the late Paleocene
788 through the early Eocene, *Paleoceanography*, 28, 650–662, doi:10.1002/palo.20060, 2013.

789 Kroeger, K. F. and Funnel, R. H.: Warm Eocene climate enhanced petroleum generation from Cretaceous source
790 rocks: a potential climate feedback mechanism?, *Geophys. Res. Lett.*, 39, L04701,
791 doi:10.1029/2011GL050345, 2012.

792 Kroenke, L., Berger, W., Janecek, T. et al.: Proceedings of the Ocean Drilling Program, Initial Reports, vol. 130,
793 Ocean Drilling Program, College Station, Texas, doi:10.2973/odp.proc.ir.130.1991, 1991.

794 Kurtz, A., Kump, L. R., Arthur, M. A., Zachos, J. C., and Paytan, A.: Early Cenozoic decoupling of the global
795 carbon and sulfur cycles, *Paleoceanography*, 18, 1090, doi:10.1029/2003PA000908, 2003.

796 Lee, C.-T. A., Shen, B., Slotnick, B. S., Liao, K., Dickens, G. R., Yokoyama, Y., Lenardic, A., Dasgupta, R.,
797 Jellinek, M., Lackey, J. S., Schneider, T., and Tice, M. M.: Continental arc–island arc fluctuations, growth of
798 crustal carbonates, and long-term climate change, *Geosphere*, 9, 21–36, doi:10.1130/GES00822.1, 2013.

799 Leech, M. L., Singh, S., Jain, A. K., Klemperer, S. L., and Manickavasagam, R. M.: The onset of India–Asia

800 continental collision: early, steep subduction required by the timing of UHP metamorphism in the western
801 Himalaya, *Earth Planet. Sc. Lett.*, 234, 83–97, 2005.

802 Lefebvre, V., Donnadieu, Y., Godd ris, Y., Fluteau, F., and Hubert-Theiou, L.: Was the Antarctic glaciation delayed
803 by a high degassing rate during the early Cenozoic?, *Earth Planet. Sc. Lett.*, 371–372, 203–211, 2013.

804 Leon-Rodr guez, L. and Dickens, G. R.: Constraints on ocean acidification associated with rapid and massive carbon
805 injections: the early Paleogene record at ocean drilling program site 1215, equatorial Pacific Ocean,
806 *Palaeogeogr. Palaeocl.*, 298, 409–420, 2010.

807 Liu, G. and Einsele, G.: Sedimentary history of the Tethyan basin in the Tibetan Himalayas, *Geol. Rundsch.*, 83, 32–
808 61, 1994.

809 Marquer, D., Mercolli, I., and Peters, T.: Early Cretaceous intra-oceanic rifting in the proto-Indian Ocean recorded
810 in the Masirah Ophiolite, Sultanate of Oman, *Tectonophysics*, 292, 1–16, 1998.

811 Massonne, H.-J.: Phase relations and dehydration behaviour of calcareous sediments at very-low to low grade
812 metamorphic conditions, *Period. Mineralogia*, 79, 21–43, 2010.

813 McCourt, W., M. Crow, E. Cobbing, and Amin, T.: Mesozoic and Cenozoic plutonic evolution of SE Asia: evidence
814 from Sumatra, Indonesia, *Special Publications, Geol. Soc. London*, 106, 321–335, 1996.

815 McQuarrie, N. and van Hinsbergen, D. J. J.: Retro-deforming the Arabia–Eurasia collision zone: age of collision
816 versus magnitude of continental subduction, *Geology*, 41, 315–318, doi:10.1130/G33591.1, 2013.

817 Menzies, M. A., Klemperer, S. L., Ebinger, C. J., and Baker, J.: Characteristics of volcanic rifted margins, in:
818 *Volcanic Rifted Margins*, 362, edited by: Menzies, M. A., Klemperer, S. L., Ebinger, C. J., and Baker, J.,
819 *Geological Society of America Special Paper*, 1–14, doi:10.1130/0-8137-2362-0.1, 2002.

820 Misra, S. and Froelich, P. N.: Lithium isotope history of Cenozoic seawater: changes in silicate weathering and
821 reverse weathering, *Science*, 335, 818–823, doi:10.1126/science.1214697, 2012.

822 Mouthereau, F.: Timing of uplift in the Zagros belt/Iranian plateau and accommodation of late Cenozoic Arabia–
823 Eurasia convergence, *Geol. Mag.*, 148, 726–738, doi:10.1017/s0016756811000306, 2011.

824 M ller, R. D., Sdrolias, M., Gaina, C., and Roest, W. R.: Age, spreading rates, and spreading asymmetry of the
825 world’s ocean crust, *Geochem. Geophys. Geosy.*, 9, Q04006, doi:10.1029/2007GC001743, 2008.

826 Muttoni, G., Mattei, M., Balini, M., Zanchi, A., Gaetani, M., and Berra, F.: The drift history of Iran from the
827 Ordovician to the Triassic, in: *South Caspian to Central Iran Basins*, edited by: Brunet, M.-F., Wilmsen, M.,

828 and Granath, J. W., Special Publications, Geological Society of London, 7–29, 2009.

829 Najman, Y., Oliver, G., Parrish, R., Vezzoli, G., Appel, E., Boudagher-Fadel, M., Bown, P., Carter, A., Garzanti, E.,
830 Godin, L., Han, J., and Liebke, U.: Timing of India–Asia collision: geological, biostratigraphic, and
831 palaeomagnetic constraints, *J. Geophys. Res.-Sol. Ea.*, 115, B12416, doi:10.1029/2010JB007673, 2010.

832 Nesbitt, B., Mendoza, C., and Kerrick, D., Surface fluid convection during cordilleran extension and the generation
833 of metamorphic CO₂ contributions to Cenozoic atmospheres, *Geology*, 23, 99–101, 1995.

834 Okay, A. I. and Şahintürk, Ö.: Geology of the Eastern Pontides, in: *Regional and Petroleum Geology of the Black*
835 *Sea and Surrounding Region*, edited by: Robinson, A. G., AAPG Memoir, 68, 291–311, 1997.

836 Orme, D. A., Carrapa, B., and Kapp, P. K.: Sedimentology, provenance and geochronology of the western Xigaze
837 Forearc, Southern Tibet, *Basin Res.*, 27, 387–411, doi:10.1111/bre.12080, 2014.

838 Pälke, H., Lyle, M.W., Nishi, H., Raffi, I., Ridgwell, A., Gamage, K., Klaus, A., Acton, G., Anderson, L.,
839 Backman, J., Baldauf, J., Beltran, C., Bohaty, S. M., Bown, P., Busch, W., Channell, J. E. T., Chun, C. O. J.,
840 Delaney, M., Dewangan, P., Dunkley Jones, T., Edgar, K. M., Evans, H., Fitch, P., Foster, G. L., Gussone, N.,
841 Hasegawa, H., Hathorne, E. C., Hayashi, H., Herrle, J. O., Holbourn, A., Hovan, S., Hyeong, K., Iijima, K., Ito,
842 T., Kamikuri, S., Kimoto, K., Kuroda, J., Leon-Rodriguez, L., Malinverno, A., Moore, T. C., Murphy, B. H.,
843 Murphy, D.P., Nakamura, H., Ogane, K., Ohneiser, C., Richter, C., Robinson, R., Rohling, E. J., Romero, O.,
844 Sawada, K., Scher, H., Schneider, L., Sluijs, A., Takata, H., Tian, J., Tsujimoto, A., Wade, B. S., Westerhold,
845 T., Wilkens, R., Williams, T., Wilson, P. A., Yamamoto, Y., Yamamoto, S., Yamazaki, T., and Zeebe, R. E.: A
846 Cenozoic record of the equatorial Pacific carbonate compensation depth, *Nature*, 488, 609–614, 2012.

847 Park, J. and Royer, D. L.: Geologic constraints on the glacial amplification of Phanerozoic climate sensitivity, *Am.*
848 *J. Sci.*, 311, 1–26, doi:10.2475/01.2011.01, 2011.

849 Peacock, S. M.: Thermal structure and metamorphic evolution of subducting slabs, in: *Inside the Subduction*
850 *Factory*, edited by: Eiler, J. M., Geophysical Monograph Ser. American Geophysical Union, Washington, D.C.,
851 7–22, 2003.

852 Raymo, M.E., and Ruddiman, W.F.: Tectonic forcing of late Cenozoic climate. *Nature*, 359, 117–122,
853 doi:10.1038/359117a0, 1992.

854 Reagan, M. K., McClelland, W. C., Girard, G., Goff, K. R., Peate, D. W., Ohara, Y., and Stern, R. J.: The geology of
855 the southern Mariana fore-arc crust: implications for the scale of Eocene volcanism in the western Pacific,

856 Earth Planet. Sc. Lett., 380, 41–51, doi:10.1016/j.epsl.2013.08.013, 2013.

857 Ricou, L. M.: Tethys reconstructed: plates, continental fragments and their boundaries since 260 Ma from Central
858 America to South-eastern Asia, *Geodin. Acta*, 7, 169–218, 1994.

859 Rohrmann, A., Kapp, P., Carrapa, B., Reiners, P. W., Guynn, J., Ding, L., and Heizler, M.: Thermochronologic
860 evidence for plateau formation in central Tibet by 45 Ma, *Geology*, 40, 187–190, doi:10.1130/G32530.1, 2012.

861 Rosenbaum, G., Lister, G. S., and Duboz, C.: Relative motions of Africa, Iberia and Europe during Alpine orogeny,
862 *Tectonophysics*, 359, 117–129, doi:10.1016/S0040-1951(02)00442-0, 2002.

863 Sanchez, V. I., Murphy, M. A., Robinson, A. C., Lapen, T. L., and Heizler, M. T.: Tectonic evolution of the India–
864 Asia suture zone since Middle Eocene time, Lopukangri area, south-central Tibet, *J. Asian Earth Sci.*, 62, 205–
865 220, 2013.

866 Sciunnach, D. and Garzanti, E.: Subsidence history of the Tethys Himalaya, *Earth-Sci. Rev.*, 25, 179–198, 2012.

867 Searle, M. and Cox, J.: Tectonic setting, origin, and obduction of the Oman ophiolite, *Geol. Soc. Am. Bull.*, 111,
868 104–122, 1999.

869 Sengör A. M. C., Altiner, D., Cin, A., Ustaömer T., and Hsü, K. J.: Origin and assembly of the Tethyside orogenic
870 collapse at the expense of Gondwana Land, in: *Gondwana and Tethys*, edited by: Audley-Charles, M. G. and
871 Hallam, A., Special Publications, Geological Society of London, 37, 119–181, 1988.

872 Shackleton, N. J. and Kennett, J. P.: Paleo-temperature history of the Cenozoic and the initiation of Antarctic
873 glaciation: oxygen and carbon isotope analyses in DSDP Sites 277, 279 and 281, *Initial Rep. Deep Sea*, 29,
874 743–755, 1975.

875 Skelton, A.: Flux rates for water and carbon during greenschist facies metamorphism, *Geology*, 39, 43–46,
876 doi:10.1130/G31328.1, 2011.

877 Slotnick, B. S., Lauretano, V., Backman, J., Dickens, G. R., Sluijs, A., and Lourens, L.: Early Paleogene variations
878 in the calcite compensation depth: new constraints using old borehole sediments from across Ninetyeast Ridge,
879 central Indian Ocean, *Clim. Past*, 11, 473–493, doi:10.5194/cp-11-473-2015, 2015.

880 Stampfli, G. M. and Borel, G. D.: A plate tectonic model for the Paleozoic and Mesozoic constrained by dynamic
881 plate boundaries and restored synthetic oceanic isochrons, *Earth Planet. Sc. Lett.*, 196, 17–33,
882 doi:10.1016/S0012-821X(01)00588-X, 2002.

883 Sykes, T. J. S.: A correction for sediment load upon the ocean floor: uniform versus varying sediment density

884 estimations – implications for isostatic correction, *Mar. Geol.*, 133, 35–49, doi:10.1016/0025-3227(96)00016-
885 3, 1996.

886 Tera, F., Brown, L., Morris, J., Sacks, I. S., Klein, J., and Middleton, R.: Sediment incorporation in island-arc
887 magmas: inferences from ^{10}Be , *Geochim. Cosmochim. Acta*, 50, 535–550, 1986.

888 Turner, S. P.: On the time-scales of magmatism at island-arc volcanoes, *Philos. T. Roy. Soc. A*, 360, 2853–2871,
889 doi:10.1098/rsta.2002.1060, 2002.

890 van Hinsbergen, D. J. J., Hafkenscheid, E., Spakman, W., Meulenkaamp, J. E., and Wortel, M. J. R.: Nappe stacking
891 resulting from subduction of oceanic and continental lithosphere below Greece, *Geology*, 33, 325–328, 2005.

892 van Hinsbergen, D. J. J., Steinberger, B., Doubrovine, P. V., and Gassmöller, R.: Acceleration and deceleration of
893 India–Asia convergence since the Cretaceous: roles of mantle plumes and continental collision, *J. Geophys.*
894 *Res.*, 116, B06101, doi:10.1029/2010JB008051,
895 2011a.

896 van Hinsbergen, D. J. J., Kapp, P., Dupont-Nivet, G., Lippert, P. C., DeCelles, P., and Torsvik, T.: Restoration of
897 Cenozoic deformation in Asia and the size of Greater India, *Tectonics*, 30, TC5003,
898 doi:10.1029/2010JB008051, 2011b.

899 van Hinsbergen, D. J. J., Lippert, P. C., Dupont-Nivet, G., McQuarrie, N., Doubrovine, P. V., Spakman, W., and
900 Torsvik, T. H.: Greater India Basin hypothesis and a two-stage Cenozoic collision between India and Asia, *P.*
901 *Natl. Acad. Sci. USA*, 109, 7659–7664, doi:10.1073/pnas.1117262109, 2012.

902 Van Der Meer, D. G., Zeebe, R. E., van Hinsbergen, D. J. J., Sluijs, A., Spakman, W., and Torsvik, T. H.: Plate
903 tectonic controls on atmospheric CO_2 levels since the Triassic, *P. Natl. Acad. Sci. USA*, 111, 4380–4385,
904 doi:10.1073/pnas.1315657111, 2014.

905 Vigier, N. and Godd eris, Y.: A new approach for modeling Cenozoic oceanic lithium isotope paleo-variations: the
906 key role of climate, *Clim. Past*, 11, 635–645, doi:10.5194/cp-11-635-2015, 2015

907 Walker, J. C. G., Hays, P. B., and Kasting, J. F.: A negative feedback mechanism for the long-term stabilization of
908 Earth’s surface temperature, *J. Geophys. Res.*, 86, 9776–9782, 1981.

909 Watts, A. B. and Thorne, J. A.: Tectonics, global changes in sea-level and their relationship to stratigraphic
910 sequences at the U.S. Atlantic continental margin, *Mar. Petrol. Geol.*, 1, 319–339, 1984.

911 Whittaker, J. M., M ller, R. D., Sdrolias, M., and Heine, C.: Sunda-Java trench kinematics, slab window formation

912 and overriding plate deformation since the Cretaceous, *Earth Planet. Sc. Lett.*, 255, 445–457,
913 doi:10.1016/j.epsl.2006.12.031, 2007.

914 Zachos, J. C., Pagani, M., Sloan, L., Thomas, E., and Billups, K.: Rhythms, and aberrations in global climate 65 Ma
915 to present, *Science*, 292, 686–693, doi:10.1126/science.1059412, 2001.

916 Zachos, J. C., Dickens, G. R., and Zeebe, R. E.: An early Cenozoic perspective on greenhouse warming and carbon-
917 cycle dynamics: year of planet Earth, *Nature*, 451, 279–283, doi:10.1038/nature06588, 2008.

918 Zheng, Y.-F.: Metamorphic chemical geodynamics in continental subduction zones, *Chem. Geol.*, 328, 5–48, 2012.

919

920

921 FIGURE CAPTIONS

922

923 **Figure 1:** Simplified paleogeographic maps showing the positions of Africa, Arabia, India and
924 Eurasia at 65, 52.5 and 35 Ma (3D Globe projection; rotation poles of **Müller et al., 2008**, fixed
925 Eurasian frame). The bearing / length of subduction trenches used in the model are represented
926 as black lines, while possible intra-oceanic subduction zones leading to obduction events (not
927 considered in the model) are reported as dashed lines. Flow lines (65-35 Ma) of three points
928 representative of the central syntaxis of each plate are also reported (see text for present
929 locations). Extension of Greater India during the Upper Cretaceous is based on the Greater India
930 Basin hypothesis of **Van Hinsbergen et al. (2012)**.

931

932 **Figure 2:** **A.** Geometry of the Eastern U.S. Atlantic coastal margin showing analogous positions
933 for tectonic units of Indian passive margin (modified from **Brookfield, 1993**). **B.** Geometry of
934 Indian margin used in **Carbonate Subduction Factory Model (CSFM)**.

935

936 **Figure 3:** Sketches illustrating the carbon input and outputs considered in the model during
937 subduction. **A.** General sketch for subduction of oceanic crust and pelagic sediments (Africa,
938 Arabia and India before Indian continental subduction). Carbon deposited as carbonate and
939 organic carbon in pelagic sediments, as well as crustal carbonate, is partly recycled at sub-arc
940 depth and incorporated in arc magmas. **B.** Similar sketch at the inset of Indian continental
941 subduction. **C.** Subduction of northern Indian margin before it reaches sub-arc depth. Carbon
942 originating from low-grade metamorphism of Indian margin sediments is partly released to the

943 atmosphere, making additional greenhouse gas to that released at arc volcanoes. **D.** Arc
944 volcanism stops as Indian continental crust reaches sub-arc depth.

945
946 **Figure 4:** **A.** Calculated mean Tethyan subduction rate over the period 65-35 Ma, compared with
947 individual subduction rates of Africa, Arabia and India beneath Eurasia. Upper and lower limits
948 of the shaded areas are maximum and minimum velocities, respectively, corresponding to points
949 located on the western and eastern syntaxes of each plate. Rates calculated using rotation
950 parameters of **van Hinsbergen et al. (2011a,b)**. **B.** Amount of CO₂ produced by the subduction
951 of the Tethys under Eurasia for the same period (green lines), using plate velocities calculated
952 from **van Hinsbergen et al. (2011a)**, for 15% and 60% efficiencies. Upper and lower limits of
953 the shaded areas are maximum and minimum gas flux rates computed for each efficiency,
954 respectively; **C.** Same as **B** but for Indian only. **D.** Same as **B** but including Indian margin
955 subduction at 55, 52.5 and 50 Ma. **E.** Same as **D** but for India only.

956
957 **Figure 5:** **A, B.** Global oceanic benthic $\delta^{18}\text{O}$ (A) and $\delta^{13}\text{C}$ (B) foraminiferal compilation based
958 on data from **Cramer et al. (2009)**. Data were smoothed using 10-point running average.
959 Temperatures calculated from $\delta^{18}\text{O}$ values assume an ice-free world (after **Komar et al. (2013)**).
960 **C.** GEOCLIM modeling results of atmospheric pCO₂ resulting from excess CO₂ release
961 associated with Neo-Tethys closure using plate velocities calculated from **van Hinsbergen et al.**
962 **(2011a)**, for 15% and 60% decarbonation efficiencies. Orange curves assume no Indian
963 continental subduction, green lines correspond to an initiation of Indian continental subduction at
964 52.5 Ma. Individual (grey diamonds) and mean (black line) atmospheric pCO₂ recorded by
965 paleoproxies are also shown (from **Beerling and Royer (2011)**). Black arrows and associated

966 number refer to pCO₂ values too high to be displayed. **D.** Same as C but for an initiation of
967 Indian continental subduction at 55 Ma (red curves) and 50 Ma (blue curves). **E.** GEOCLIM
968 modeling results of atmospheric pCO₂ resulting from excess CO₂ release as calculated from data
969 of **Kent and Muttoni (2013)** using efficiencies of 10%, 15% and 60%.
970

971 FIGURE CAPTIONS

972

973 **Figure 1:** Simplified paleogeographic maps showing the positions of Africa, Arabia, India and
974 Eurasia at 65, 52.5 and 35 Ma (3D Globe projection; rotation poles of **Müller et al., 2008**, fixed
975 Eurasian frame). The bearing / length of subduction trenches used in the model are represented
976 as black lines, while possible intra-oceanic subduction zones leading to obduction events (not
977 considered in the model) are reported as dashed lines. Flow lines (65-35 Ma) of three points
978 representative of the central syntaxis of each plate are also reported (see text for present
979 locations). Extension of Greater India during the Upper Cretaceous is based on the Greater India
980 Basin hypothesis of **Van Hinsbergen et al. (2012)**.

981

982 **Figure 2:** **A.** Geometry of the Eastern U.S. Atlantic coastal margin showing analogous positions
983 for tectonic units of Indian passive margin (modified from **Brookfield, 1993**). **B.** Geometry of
984 Indian margin used in **Carbonate Subduction Factory Model (CSFM)**.

985

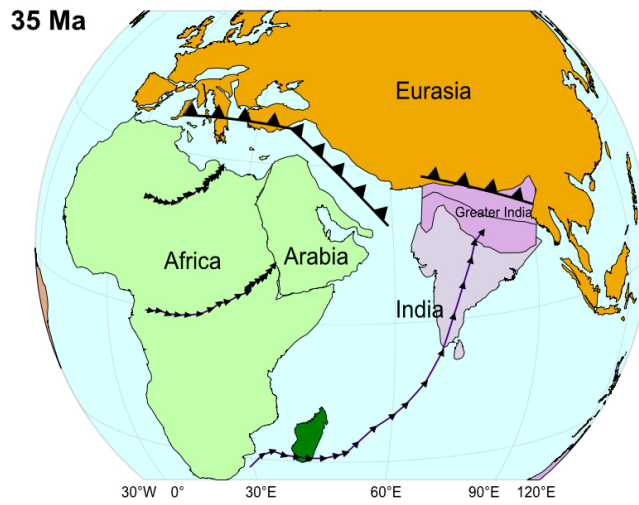
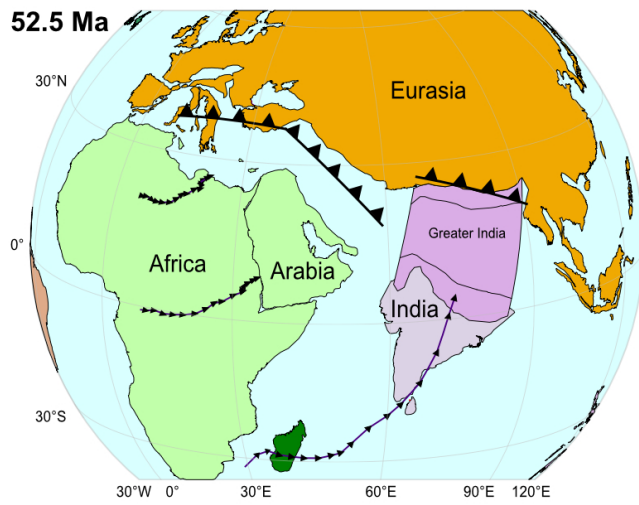
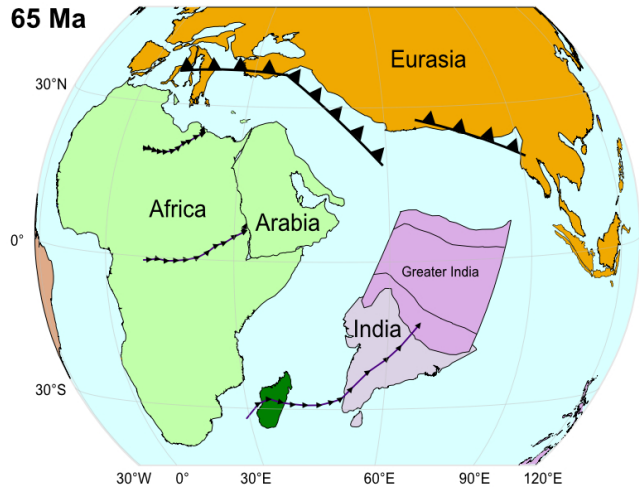
986 **Figure 3:** Sketches illustrating the carbon input and outputs considered in the model during
987 subduction. **A.** General sketch for subduction of oceanic crust and pelagic sediments (Africa,
988 Arabia and India before Indian continental subduction). Carbon deposited as carbonate and
989 organic carbon in pelagic sediments, as well as crustal carbonate, is partly recycled at sub-arc
990 depth and incorporated in arc magmas. **B.** Similar sketch at the inset of Indian continental
991 subduction. **C.** Subduction of northern Indian margin before it reaches sub-arc depth. Carbon
992 originating from low-grade metamorphism of Indian margin sediments is partly released to the

993 atmosphere, making additional greenhouse gas to that released at arc volcanoes. **D.** Arc
994 volcanism stops as Indian continental crust reaches sub-arc depth.

995
996 **Figure 4: A.** Calculated mean Tethyan subduction rate over the period 65-35 Ma, compared with
997 individual subduction rates of Africa, Arabia and India beneath Eurasia. Upper and lower limits
998 of the shaded areas are maximum and minimum velocities, respectively, corresponding to points
999 located on the western and eastern syntaxes of each plate. Rates calculated using rotation
1000 parameters of **van Hinsbergen et al. (2011a,b)**. **B.** Amount of CO₂ produced by the subduction
1001 of the Tethys under Eurasia for the same period (green lines), using plate velocities calculated
1002 from **van Hinsbergen et al. (2011a)**, for 15% and 60% efficiencies. Upper and lower limits of
1003 the shaded areas are maximum and minimum gas flux rates computed for each efficiency,
1004 respectively; **C.** Same as **B** but for Indian only. **D.** Same as **B** but including Indian margin
1005 subduction at 55, 52.5 and 50 Ma. **E.** Same as **D** but for India only.

1006
1007 **Figure 5: A, B.** Global oceanic benthic $\delta^{18}\text{O}$ (A) and $\delta^{13}\text{C}$ (B) foraminiferal compilation based
1008 on data from **Cramer et al. (2009)**. Data were smoothed using 10-point running average.
1009 Temperatures calculated from $\delta^{18}\text{O}$ values assume an ice-free world (after **Komar et al. (2013)**).
1010 **C.** GEOCLIM modeling results of atmospheric pCO₂ resulting from excess CO₂ release
1011 associated with Neo-Tethys closure using plate velocities calculated from **van Hinsbergen et al.**
1012 **(2011a)**, for 15% and 60% decarbonation efficiencies. Orange curves assume no Indian
1013 continental subduction, green lines correspond to an initiation of Indian continental subduction at
1014 52.5 Ma. Individual (grey diamonds) and mean (black line) atmospheric pCO₂ recorded by
1015 paleoproxies are also shown (from **Beerling and Royer (2011)**). Black arrows and associated

1016 number refer to pCO₂ values too high to be displayed. **D.** Same as C but for an initiation of
1017 Indian continental subduction at 55 Ma (red curves) and 50 Ma (blue curves). **E.** GEOCLIM
1018 modeling results of atmospheric pCO₂ resulting from excess CO₂ release as calculated from data
1019 of **Kent and Muttoni (2013)** using efficiencies of 10%, 15% and 60%.
1020

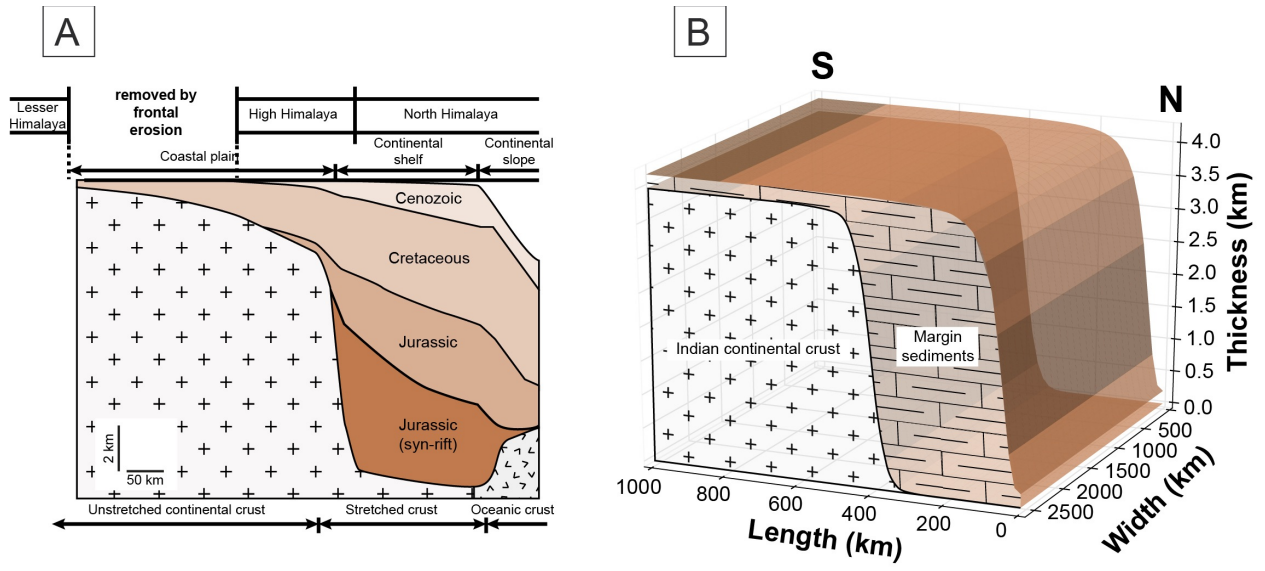


1021

1022

1023 FIGURE 1

1024

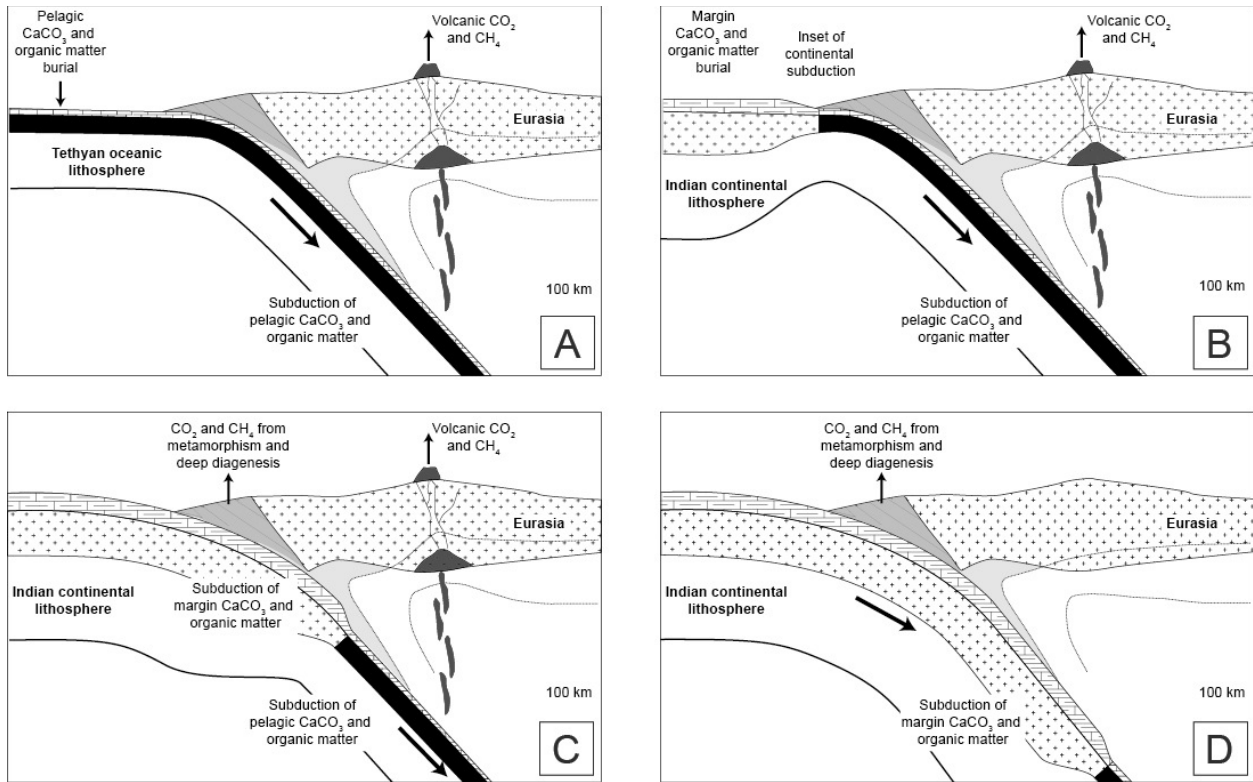


1025

1026 FIGURE 2

1027

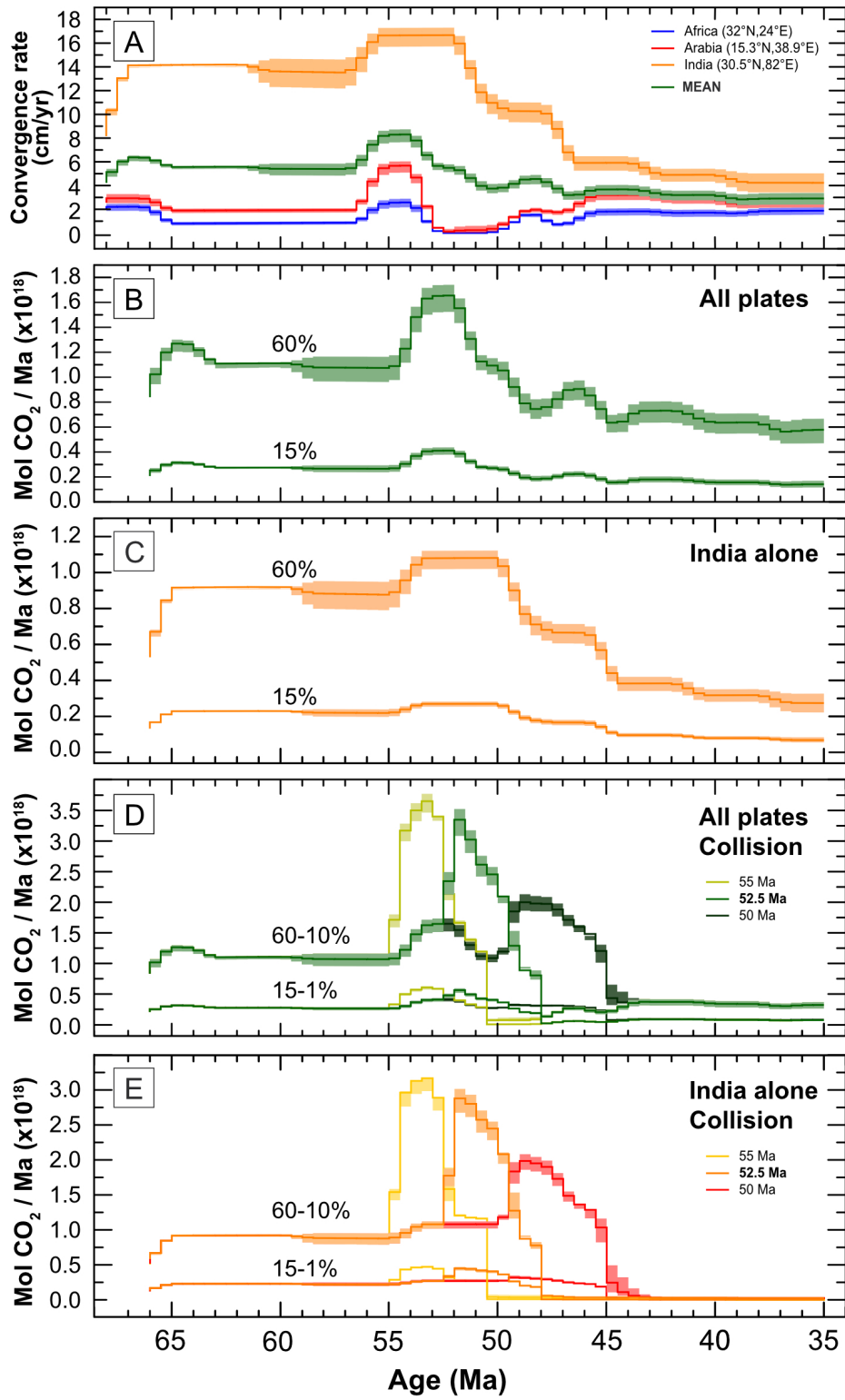
1028

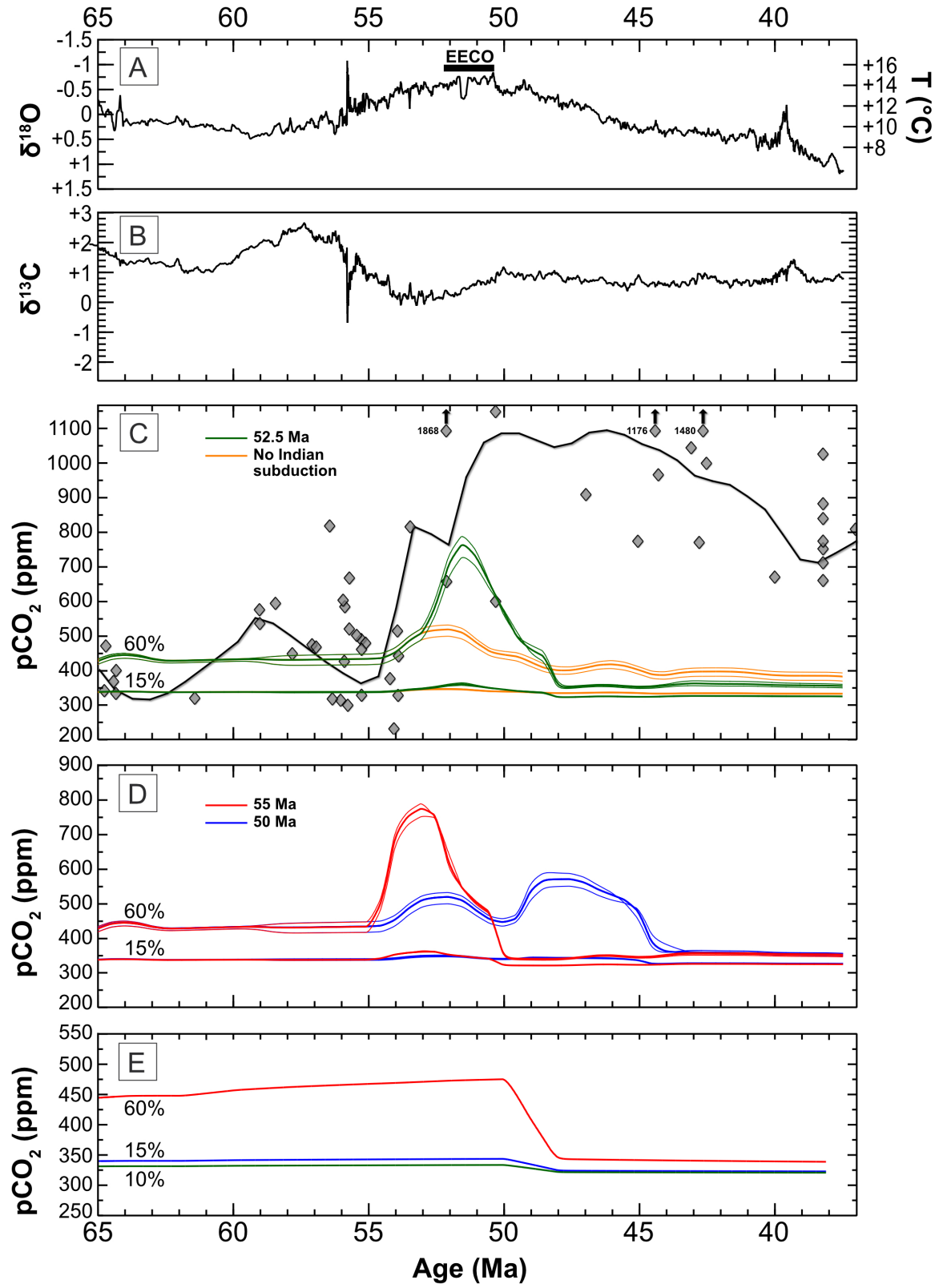


1029

1030 FIGURE 3

1031





1035

1036 FIGURE 5